A Method of Field Expansions for Multiply Layered Media with Quasiperiodic Interfaces

DAVID P. NICHOLLS[1,*]

[1] *Department of Mathematics, Statistics, and Computer Science, University of Illinois at Chicago, Chicago, IL 60607, USA*
[*] *davidn@uic.edu*

Abstract: Periodic structures are foundational in applied optics, however, more permissive forms of periodicity are becoming increasingly important in electromagnetics. Due both to their central importance and the high cost of their production at nanoscale, numerical approximation of scattering by such structures is very important. In this paper the author derives, implements, and validates the generalization of the Method of Field Expansions (FE), a classical High–Order Perturbation of Surfaces (HOPS) algorithm, to numerically simulate multiply layered media scattering in the presence of quasiperiodic interfaces. This interfacial HOPS approach is not only substantially faster for layered media configurations than its volumetric counterparts (e.g., Finite Difference or Finite Element Methods), but also useful for structures which the classical FE method would find severely challenging (for interfaces with widely disparate periods) or impossible (for profiles of incommensurate periods) due to its enhanced capability of simulating quasiperiodic interfaces. With an implementation of this algorithm, the author investigates the (nonlinear) dispersion relation of Surface Plasmon Resonances on several increasingly difficult, alternately vacuum–silver, multiply layered structures with quasiperiodic interfaces.

1. Introduction

Structures featuring periodic patterning are crucially important in applied optics, e.g., photonic crystals [1, 2]. Such exactly patterned materials enable the design of crystals which can give desired reflectance and transmittance properties effectively enabling fully guided light flow [2]. Periodicity also features in other applications in optics, for instance the Surface Plasmon Resonances (SPRs) generated by metallic diffraction gratings [3–5] which are of note due to not only their theoretical interest but also their applied importance, e.g., as sensors [6–12].

Due to the significance of these devices, the whole collection of classical algorithms for the simulation of partial differential equations has been brought to bear on their estimation [13, 14]. This includes the Finite Difference Time Domain (FDTD) Method [15], the Finite Difference Frequency Domain (FDFD) Method [16], the Finite Element Method (FEM) [17], and the Discontinuous Galerkin (DG) Method [18]. Bespoke methods have also been invented specifically for the governing Helmholtz/Maxwell equations, e.g., the Planewave Eigensolver [19, 20], the Rigorous Coupled–Wave Analysis (RCWA) [21, 22], the Fourier Modal Method (FMM) [23], and the Discrete Dipole Method [24]. While each of these is an enticing approach for quite general structures, their *volumetric* nature renders them non–competitive for layered gratings separated by sharp interfaces. For these, *surface* methods are more efficient, and paramount among these are the Boundary Integral Method [25], the Boundary Element Method [26, 27] (accelerated by the Fast Multipole Method [28–30]), and the Method of Moments [31].

In this contribution we consider other members of this class, namely the interfacial High–Order Perturbation of Surface (HOPS) methods: The method of Operator Expansions (OE) due to Milder [32–38], the method of Field Expansions (FE) due to Bruno & Reitich [39–44], and the method of Transformed Field Expansions (TFE) due to the author and Reitich [45–51]. While all are amenable to such generalizations, this latter method has been significantly enhanced to accommodate multiple layers and the full three–dimensional vector Maxwell equations by He, Min, Shen, and the author [52, 53] and Hong and the author [54–56]. Beyond this, the

TFE method was rigorously numerically analyzed in [57, 58] and HOPS schemes have been shown to be rapid, robust, and reliable in simulating scattering returns by layered media with sharp interfaces. Due to their perturbative nature, they are most compelling for configurations with interfaces that are small (in amplitude and/or slope) and smooth (e.g., analytic). However, they can also be applied to large and rough (e.g., Lipschitz) interfaces with numerical analytic continuation techniques (e.g., Padé summation [59]). This has been justified with rigorous results [47, 49] which demonstrate that perturbations of *arbitrary* size can be accommodated provided that they are *real*.

The precise patterning of these periodic diffraction gratings is crucial to generating the phenomena which justify their use in engineering devices (e.g., band gaps, plasmonic hot spots), however, they are extremely costly and difficult to fabricate [60]. Furthermore, it is now becoming evident that "nearly" periodic devices may have their own interesting properties worthy of consideration in future devices, for instance the "magic angle" Moiré patterning of multiply layered graphene [61–66].

Naturally, removing strict periodicity requirements raises the challenging question of their replacements. In the current work we study the notion of "quasiperiodicity" championed by Moser [67] and utilized by Wilkening and Zhao [68–71] in the context of the free–surface fluid mechanical water wave problem. (See also the recent paper [72].) More specifically, we continue the recent work of the author [73] and extend his FE algorithm for a *single* quasiperiodic interface to *multiple* layers in the two–dimensional setting. This highly nontrivial extension is not merely of theoretical interest as it will allow the faithful simulation of the much more realistic devices which are not only of *finite* vertical extent, but also consist of layers of *many* different materials. Here we will demonstrate how complex gratings with several different layers featuring widely disparate or even incommensurate periodicities can be simulated with ease. This will be accomplished with a simple, accurate, and robust reformulation of the governing equations involving dependent variables simply "lifted" to a higher dimensional torus. Before proceeding, we note that our scheme is related to the work of Lou & Fan [66] who implemented a generalization of the RCWA very much akin to what we propose. While we only address two dimensional configurations (TE/TM polarization), we intend to generalize our algorithm to both the fully vectorial Maxwell equations in three dimensions, and two dimensional periodic materials (such as graphene) to simulate Moiré patterning.

The paper is organized as follows: In Section 2 we state the equations governing the linear scattering of electromagnetic radiation by a multiply–layered grating with a sharp interfaces. In Section 3 we recall Moser's definition of quasiperiodic functions used in this paper and in Section 3.1 we specify the generalized Rayleigh expansions for linear waves satisfying these quasiperiodic boundary conditions. In Section 4 we outline our new FE recursions for quasiperiodic interfaces. In Section 5 we detail our numerical results which includes a discussion of algorithmic details for the FE approach in Section 5.1 and validation experiments in Section 5.2. In Sections 5.3 and 5.4 we discuss a sequence of numerical simulations where we computed the absorbance of radiation incident upon three–layer (Section 5.3) and five–layer (Section 5.4) gratings with small, but non–trivial, quasiperiodic interfaces, as a function of interface wavenumber and radiation frequency, resulting in "nonlinear dispersion relations" of SPRs [3–5, 74, 75]. We give concluding remarks and discuss future directions in Section 6.

2. The Governing Equations

We consider in this paper structures with the geometry displayed in Figure 1: A y–invariant, multiply layered diffraction grating with sharp interfaces, specified by the graphs of the functions

$z = a^{(m)} + g^{(m)}(x)$, $1 \leq m \leq M$, separating $(M+1)$ materials which define the domains

$$
\begin{aligned}
S^{(0)} &:= \left\{ (x,z) \mid z > a^{(1)} + g^{(1)}(x) \right\}, \\
S^{(m)} &:= \left\{ (x,z) \mid a^{(m+1)} + g^{(m+1)}(x) < z < a^{(m)} + g^{(m)}(x) \right\}, \qquad 1 \leq m \leq M-1, \\
S^{(M)} &:= \left\{ (x,z) \mid z < a^{(M)} + g^{(M)}(x) \right\},
\end{aligned}
$$

with upward pointing normals

$$N^{(m)} = (-\partial_x g^{(m)}(x), 1)^T, \quad 1 \leq m \leq M.$$

The layers are filled with homogeneous materials of permittivities $\epsilon^{(m)}$, $0 \leq m \leq M$, where $\epsilon^{(0)} \in \mathbf{R}^+$ indicating a dielectric. The structure is illuminated from above by monochromatic plane–wave incident radiation of frequency ω and wavenumber $k^{(0)} = \sqrt{\epsilon^{(0)}}\omega/c_0$ (c_0 is the speed of light) aligned with the grooves

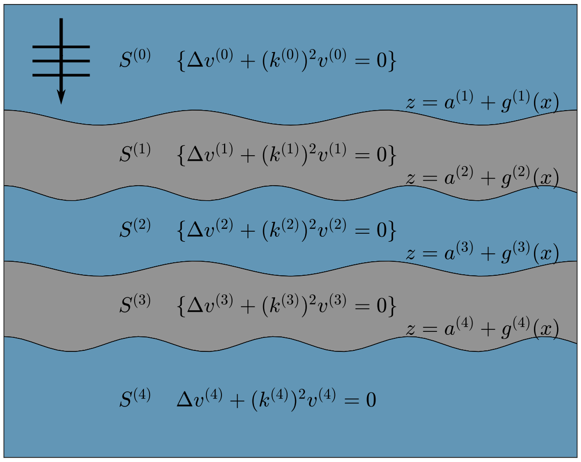

Fig. 1. A multiply-layered structure with interfaces, $z = a^{(m)} + g^{(m)}(x)$, $1 \leq m \leq M$, separating $(M+1)$ material layers, $S^{(m)}$, illuminated by plane–wave incidence.

$$
\begin{gathered}
\underline{\mathbf{E}}^i(x,z,t) = \mathbf{A} e^{-i\omega t + i\alpha x - i\gamma^{(0)} z}, \quad \underline{\mathbf{H}}^i(x,z,t) = \mathbf{B} e^{-i\omega t + i\alpha x - i\gamma^{(0)} z}, \\
\alpha := k^{(0)} \sin(\theta), \quad \gamma^{(0)} := k^{(0)} \cos(\theta).
\end{gathered}
$$

We study reduced fields where time dependence $\exp(-i\omega t)$ and lateral spatial phase $\exp(i\alpha x)$ have been factored out, e.g.,

$$\mathbf{E}(x,z) = e^{i\omega t} e^{-i\alpha x} \underline{\mathbf{E}}(x,z,t), \quad \mathbf{H}(x,z) = e^{i\omega t} e^{-i\alpha x} \underline{\mathbf{H}}(x,z,t),$$

which measure the scattered electric and magnetic fields, respectively. It is known [76, 77] that in this two–dimensional setting, the time–harmonic Maxwell equations decouple into two scalar Helmholtz problems which govern the Transverse Electric (TE) and Transverse Magnetic (TM) polarizations. Denoting the invariant (y) direction of the scattered (electric or magnetic) field in $S^{(m)}$ by $v^{(m)}(x,z)$ we have

$$\Delta v^{(m)} + 2i\alpha\partial_x v^{(m)} + (\gamma^{(m)})^2 v^{(m)} = 0, \quad \text{in } S^{(m)}, \quad 0 \leq m \leq M, \tag{1}$$

where

$$(\gamma^{(m)})^2 = \epsilon^{(m)} k_0^2 - \alpha^2, \quad 0 \leq m \leq M.$$

Continuity of the fields at the interfaces demands

$$v^{(m-1)} - v^{(m)} = \xi^{(m)}, \qquad z = a^{(m)} + g^{(m)}(x), \tag{2a}$$

$$\tau^{(m-1)} \mathcal{N}^{(m)} v^{(m-1)} - \tau^{(m)} \mathcal{N}^{(m)} v^{(m)} = \tau^{(m-1)} \nu^{(m)}, \qquad z = a^{(m)} + g^{(m)}(x), \tag{2b}$$

for $1 \leq m \leq M$, where

$$\mathcal{N}^{(m)} := \partial_z - (\partial_x g^{(m)})\partial_x - i\alpha(\partial_x g^{(m)}), \quad 1 \leq m \leq M,$$

and the Dirichlet and Neumann data are

$$\xi^{(1)}(x) = -e^{-i\gamma^{(0)}(a^{(1)}+g^{(1)}(x))}, \quad \nu^{(1)}(x) = \left\{ i\gamma^{(0)} + i\alpha(\partial_x g^{(1)}(x)) \right\} e^{-i\gamma^{(0)}(a^{(1)}+g^{(1)}(x))},$$
$$\xi^{(m)}(x) \equiv 0, \quad \nu^{(m)}(x) \equiv 0, \quad 2 \leq m \leq M,$$

and

$$\tau^{(m)} = \begin{cases} 1, & \text{TE}, \\ 1/\epsilon^{(m)}, & \text{TM}. \end{cases}$$

To close the problem, we specify that the scattered radiation is outgoing: Upward propagating in $S^{(0)}$ and downward propagating in $S^{(M)}$.

3. Quasiperiodic Functions

To study new phenomena when plane waves are scattered by gratings with more general periodicity we utilize the notion of quasiperiodicity. Among several definitions which have been proposed, we choose the one advocated by Moser [67] and define a function $f(x)$ to be quasiperiodic if

$$f(x) = \tilde{f}(X), \quad X = Kx, \quad x \in \mathbf{R}^d, \quad X \in \mathbf{R}^D, \quad K \in \mathbf{R}^{D \times d},$$

and the envelope function $\tilde{f}(X)$ is *periodic* with respect to the lattice

$$\Gamma = (2\pi\mathbf{Z})^D.$$

Here we have the Fourier series representation

$$\tilde{f}(X) = \sum_{p \in \Gamma'} \hat{f}_p e^{ip\cdot X}, \quad \hat{f}_p = \frac{1}{(2\pi)^D} \int_{P(\Gamma)} \tilde{f}(X) e^{-ip\cdot X}\, dX,$$

where

$$\Gamma' = \mathbf{Z}^D, \quad P(\Gamma) = [0, 2\pi)^D.$$

Notice that if $d = D$ and K is invertible then the function $f(x)$ is periodic with respect to the lattice induced by K. We observe that

$$\nabla_x f = K^T \nabla_X \tilde{f}, \quad \Delta_x f = \text{div}_X \left[K K^T \nabla_X \tilde{f} \right].$$

To prescribe a truly non–periodic function one must specify $D > d$ and that the rows of K be linearly independent over the integers. To appreciate this latter point, we consider the case $d = 1$ and $D = 2$, which will be our focus in this work, and select

$$K = (1, q/r)^T, \quad q, r \in \mathbf{Z},$$

featuring rational entries. With the calculation

$$f(x + 2\pi r) = \tilde{f}(x + 2\pi r, (q/r)(x + 2\pi r)) = \tilde{f}(x + 2\pi r, (q/r)x + 2\pi q) = \tilde{f}(x, (q/r)x) = f(x),$$

it is clear that $f(x)$ is, in fact, $(2\pi r)$–periodic. A simple example of a non–periodic quasiperiodic function (when $d = 1$ and $D = 2$) can be specified by

$$K = (1, \kappa)^T, \quad \kappa \notin \mathbf{Q}.$$

We note that the second and fourth interfaces, $z = a^{(2)} + g^{(2)}(x)$ and $z = a^{(4)} + g^{(4)}(x)$, depicted in Figure 1 are quasiperiodic with $\kappa = \sqrt{2}$. The generating envelope function $\tilde{g}(X) = \tilde{g}(X_1, X_2) = \cos(X_1) + \cos(X_2)$ is shown in Figure 2 together with the line $X_2 = \kappa X_1 = \sqrt{2} X_1$ along which $\tilde{g}(X)$ is sampled to give $g^{(2)}(x)$ and $g^{(4)}(x)$ [73].

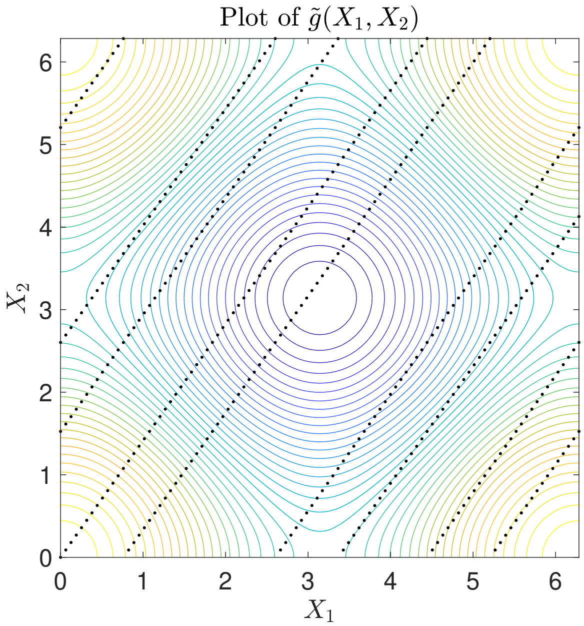

Fig. 2. A contour plot of the envelope function $\tilde{g}(X) = \tilde{g}(X_1, X_2) = \cos(X_1) + \cos(X_2)$ overlaid with the line $X_2 = \kappa X_1 = \sqrt{2} X_1$ along which $z = \tilde{g}(X)$ is sampled to give the interfaces in Figure 1.

These definitions can be naturally extended to functions which are both laterally quasiperiodic and vertically varying, e.g., $v^{(m)} = v^{(m)}(x, z)$. More specifically, we define such a function to be laterally quasiperiodic if

$$v^{(m)}(x, z) = \tilde{v}^{(m)}(X, z), \quad X = Kx, \quad x \in \mathbf{R}^d, \quad X \in \mathbf{R}^D, \quad K \in \mathbf{R}^{D \times d},$$

and the envelope function $\tilde{v}^{(m)}(X, z)$ is laterally *periodic* with respect to the lattice Γ above. Once again, we have the Fourier series representation

$$\tilde{v}^{(m)}(X, z) = \sum_{p \in \Gamma'} \hat{v}_p^{(m)}(z) e^{ip \cdot X}, \quad \hat{v}_p^{(m)}(z) = \frac{1}{(2\pi)^D} \int_{P(\Gamma)} \tilde{v}(X, z) e^{-ip \cdot X} \, dX.$$

We now assume that the interfaces

$$z = a^{(m)} + g^{(m)}(x) = a^{(m)} + \tilde{g}^{(m)}(X), \quad 1 \leq m \leq M,$$

are quasiperiodic and seek laterally quasiperiodic scattered fields

$$v^{(m)}(x, z) = \tilde{v}^{(m)}(X, z), \quad 0 \leq m \leq M,$$

satisfying the Helmholtz equations (1), Dirichlet conditions (2a), and Neumann conditions (2b). Thus, we require Γ–periodic, upward/downward propagating solutions of

$$\begin{aligned}
&\tilde{\mathcal{L}}^{(m)} \tilde{v}^{(m)} = 0, && \text{in } S^{(m)}, 0 \leq m \leq M, && \text{(3a)}\\
&\tilde{v}^{(m-1)} - \tilde{v}^{(m)} = \tilde{\xi}^{(m)}, && z = a^{(m)} + \tilde{g}^{(m)}(X), 1 \leq m \leq M, && \text{(3b)}\\
&\tau^{(m-1)} \tilde{\mathcal{N}}^{(m)} \tilde{v}^{(m-1)} - \tau^{(m)} \tilde{\mathcal{N}}^{(m)} \tilde{v}^{(m)} = \tau^{(m-1)} \tilde{\nu}^{(m)}, && z = a^{(m)} + \tilde{g}^{(m)}(X), 1 \leq m \leq M, && \text{(3c)}
\end{aligned}$$

where

$$\begin{aligned}
\tilde{\mathcal{L}}^{(m)} &:= \operatorname{div}_X \left[K K^T \nabla_X \right] + \partial_z^2 + 2 i \alpha K^T \nabla_X + (\gamma^{(m)})^2,\\
\tilde{\mathcal{N}}^{(m)} &:= \partial_z - (K^T \nabla_X \tilde{g}^{(m)}) \cdot (K^T \nabla_X) - i \alpha \cdot (K^T \nabla_X \tilde{g}^{(m)}),
\end{aligned}$$

and

$$\tilde{\xi}^{(1)}(X) = -e^{-i\gamma^{(0)} (a^{(1)} + \tilde{g}^{(1)})}, \quad \tilde{\nu}^{(1)}(X) = \left\{ (i\gamma^{(0)}) + i\alpha \cdot (K^T \nabla_X \tilde{g}^{(1)}) \right\} e^{-i\gamma^{(0)} (a^{(1)} + \tilde{g}^{(1)})},$$

$$\tilde{\xi}^{(m)}(X) \equiv 0, \quad \tilde{\nu}^{(m)}(X) \equiv 0, \quad 2 \leq m \leq M.$$

3.1. *The Rayleigh Expansions*

At this point it is crucial that we recall the Rayleigh expansions, derived from separation of variables [76, 77], which specify the Γ–periodic, upward/downward propagating solutions of (3a). More specifically, these are

$$\tilde{v}^{(m)}(X, z) = \sum_{p \in \Gamma'} \left\{ d_p^{(m)} e^{-i\gamma_p^{(m)} (z - a^{(m)})} + u_p^{(m)} e^{i\gamma_p^{(m)} (z - a^{(m+1)})} \right\} e^{i p \cdot X}, \quad 0 \leq m \leq M, \tag{4}$$

where, for $\alpha \in \mathbf{R}^d$, $p \in \mathbf{Z}^D$,

$$\alpha_p := \alpha + K^T p, \quad \gamma_p^{(m)} := \sqrt{\epsilon^{(m)} k_0^2 - \left| \alpha_p \right|^2}, \quad \operatorname{Im}\{\gamma_p^{(m)}\} \geq 0.$$

In the case $\epsilon^{(m)} \in \mathbf{R}^+$ we have

$$\gamma_p^{(m)} = \begin{cases} \sqrt{\epsilon^{(m)} k_0^2 - \left| \alpha_p \right|^2}, & p \in \mathcal{U}^{(m)}, \\ i \sqrt{\left| \alpha_p \right|^2 - \epsilon^{(m)} k_0^2}, & p \notin \mathcal{U}^{(m)}, \end{cases}$$

where

$$\mathcal{U}^{(m)} := \left\{ p \in \mathbf{Z}^D \mid \left| \alpha_p \right|^2 < \epsilon^{(m)} k_0^2 \right\},$$

which are the propagating modes. The upward propagating condition in the upper layer and the downward propagating condition in the lower layer demand that

$$d_p^{(0)} \equiv 0, \quad u_p^{(M)} \equiv 0, \quad p \in \Gamma'.$$

In the case of *all* flat interfaces, $\tilde{g}^{(m)}(X) \equiv 0$, these Rayleigh expansions can be used to recover the exact solution of (3). More specifically, the boundary conditions, (3b) & (3c), reduce, at each wavenumber $p \in \Gamma'$, to

$$\mathbf{A}_p \vec{V}_p = \vec{R}_p, \tag{5a}$$

where

$$\mathbf{A}_p := \begin{pmatrix}
\underline{\mathbf{U}}^{(0)} & \overline{\mathbf{D}}^{(1)} & \overline{\mathbf{U}}^{(1)} & & & & \\
 & \underline{\mathbf{D}}^{(1)} & \underline{\mathbf{U}}^{(1)} & \overline{\mathbf{D}}^{(2)} & \overline{\mathbf{U}}^{(2)} & & \\
 & & \ddots & \ddots & \ddots & \ddots & \\
 & & & \underline{\mathbf{D}}^{(M-2)} & \underline{\mathbf{U}}^{(M-2)} & \overline{\mathbf{D}}^{(M-1)} & \overline{\mathbf{U}}^{(M-1)} & \\
 & & & & & \underline{\mathbf{D}}^{(M-1)} & \underline{\mathbf{U}}^{(M-1)} & \overline{\mathbf{D}}^{(M)}
\end{pmatrix}, \tag{5b}$$

and

$$\underline{\mathbf{U}}^{(m)} = \begin{pmatrix} 1 \\ \tau^{(m)}(i\gamma_p^{(m)}) \end{pmatrix}, \qquad 0 \le m \le M-1, \tag{5c}$$

$$\underline{\mathbf{D}}^{(m)} = \begin{pmatrix} \Gamma_p^{(m)} \\ \tau^{(m)}(-i\gamma_p^{(m)})\Gamma_p^{(m)} \end{pmatrix}, \qquad 1 \le m \le M-1, \tag{5d}$$

$$\overline{\mathbf{U}}^{(m)} = \begin{pmatrix} -\Gamma_p^{(m)} \\ -\tau^{(m)}(i\gamma_p^{(m)})\Gamma_p^{(m)} \end{pmatrix}, \qquad 1 \le m \le M-1, \tag{5e}$$

$$\overline{\mathbf{D}}^{(m)} = \begin{pmatrix} -1 \\ -\tau^{(m)}(-i\gamma_p^{(m)}) \end{pmatrix}, \qquad 1 \le m \le M, \tag{5f}$$

and

$$\Gamma_p^{(m)} := e^{i\gamma_p^{(m)}h^{(m)}}, \quad h^{(m)} := a^{(m)} - a^{(m+1)}, \quad 1 \le m \le M-1, \tag{5g}$$

and

$$\vec{V}_p = \begin{pmatrix} u_p^{(0)} \\ d_p^{(1)} \\ u_p^{(1)} \\ \vdots \\ d_p^{(M-1)} \\ u_p^{(M-1)} \\ d_p^{(M)} \end{pmatrix}, \quad \vec{R}_p = \begin{pmatrix} \hat{\xi}_p^{(1)} \\ \tau^{(0)}\hat{\nu}_p^{(1)} \\ \hat{\xi}_p^{(2)} \\ \vdots \\ \tau^{(M-2)}\hat{\nu}_p^{(M-1)} \\ \hat{\xi}_p^{(M)} \\ \tau^{(M-1)}\hat{\nu}_p^{(M)} \end{pmatrix}, \tag{5h}$$

which can be readily solved via Gaussian elimination. Once $\vec{V}_p$ has been recovered, one can produce quantities of interest such as the reflectance, R, and transmission, T. In fact, in this case of planewave incidence

$$\hat{\xi}_0^{(1)} = -1; \quad \hat{\nu}_0^{(1)} = i\gamma^{(0)}; \quad \hat{\xi}_p^{(1)} = \hat{\nu}_p^{(1)} = 0, \quad p \neq 0;$$

we recover the Fresnel coefficients [76] giving the reflectance and transmission

$$R = u_0^{(0)} e^{-i\gamma^{(0)}a^{(1)}}, \quad T = d_0^{(M)} e^{i\gamma^{(M)}a^{(M)}}.$$

This elementary solution procedure is used repeatedly at the heart of the FE algorithm.

4. The Method of Field Expansions

High–Order Perturbation of Surfaces (HOPS) methods are perturbation algorithms where the expansion variable, ε, comes from the interfacial deformations. In the present case these are of the form $z = a^{(m)} + \tilde{g}^{(m)}(X) = a^{(m)} + \varepsilon \tilde{f}^{(m)}(X)$ and we initially assume that ε is small. However, it is important to note that the actual domain of analyticity usually includes a neighborhood of the *entire* real axis (see, e.g., [47, 49]) meaning that *large* (but real) deformations can be considered with analytic continuation methods. (The method of Padé approximation [59] is a particularly compelling choice for this task.) In this work we study a particular HOPS approach, namely the method of Field Expansions (FE) [39–41].

In the present context, the FE method begins with the expansions

$$\tilde{v}^{(m)} = \tilde{v}^{(m)}(X, z; \varepsilon) = \sum_{n=0}^{\infty} \tilde{v}_n^{(m)}(X, z)\varepsilon^n, \quad 0 \leq m \leq M,$$

and inserts these into (3) and, equating at equal orders of ε, results in

$$\begin{aligned} &\tilde{\mathcal{L}}^{(m)} \tilde{v}_n^{(m)} = 0, && \text{in } S^{(m)}, 0 \leq m \leq M, && \text{(6a)} \\ &\tilde{v}_n^{(m-1)} - \tilde{v}_n^{(m)} = \tilde{\xi}_n^{(m)} + \tilde{Q}_n^{(m)}, && z = a^{(m)}, 1 \leq m \leq M, && \text{(6b)} \\ &\tau^{(m-1)} \partial_z \tilde{v}_n^{(m-1)} - \tau^{(m)} \partial_z \tilde{v}_n^{(m)} = \tau^{(m-1)} \tilde{\nu}_n^{(m)} + \tilde{R}_n^{(m)}, && z = a^{(m)}, 1 \leq m \leq M, && \text{(6c)} \end{aligned}$$

where

$$\tilde{\xi}_n^{(1)}(X) = -(-i\gamma^{(0)})^n \tilde{F}_n^{(m)} e^{-i\gamma^{(0)} a^{(1)}},$$

$$\tilde{\nu}_n^{(1)}(X) = (i\gamma^{(0)}) \left\{ (-i\gamma^{(0)})^n \tilde{F}_n^{(m)} + i\alpha(-i\gamma^{(0)})^{n-1} (K^T \nabla_X \tilde{f}^{(1)}) \tilde{F}_{n-1}^{(m)} \right\} e^{-i\gamma^{(0)} a^{(1)}},$$

$$\tilde{\xi}_n^{(m)}(X) \equiv 0, \quad \tilde{\nu}_n^{(m)}(X) \equiv 0, \quad 2 \leq m \leq M.$$

Additionally, for $1 \leq m \leq M$,

$$\tilde{Q}_n^{(m)} = -\sum_{\ell=0}^{n-1} \tilde{F}_{n-\ell}^{(m)} \partial_z^{n-\ell} \tilde{v}_\ell^{(m-1)}(X, a^{(m)}) + \sum_{\ell=0}^{n-1} \tilde{F}_{n-\ell}^{(m)} \partial_z^{n-\ell} \tilde{v}_\ell^{(m)}(X, a^{(m)}), \tag{7}$$

and, for $1 \leq m \leq M$,

$$\begin{aligned} \tilde{R}_n^{(m)} = &-\tau^{(m-1)} \sum_{\ell=0}^{n-1} \tilde{F}_{n-\ell}^{(m)} \partial_z^{n-\ell+1} \tilde{v}_\ell^{(m-1)}(X, a^{(m)}) \\ &+ \tau^{(m-1)} \sum_{\ell=0}^{n-1} \tilde{F}_{n-1-\ell}^{(m)} (K^T \nabla_X \tilde{f}^{(m)}) \cdot K^T \nabla_X \partial_z^{n-1-\ell} \tilde{v}_\ell^{(m-1)}(X, a^{(m)}) \\ &+ \tau^{(m-1)} \sum_{\ell=0}^{n-1} \tilde{F}_{n-1-\ell}^{(m)} (i\alpha) \cdot (K^T \nabla_X \tilde{f}^{(m)}) \partial_z^{n-1-\ell} \tilde{v}_\ell^{(m-1)}(X, a^{(m)}) \\ &+ \tau^{(m)} \sum_{\ell=0}^{n-1} \tilde{F}_{n-\ell}^{(m)} \partial_z^{n-\ell+1} \tilde{v}_\ell^{(m)}(X, a^{(m)}) \\ &- \tau^{(m)} \sum_{\ell=0}^{n-1} \tilde{F}_{n-1-\ell}^{(m)} (K^T \nabla_X \tilde{f}^{(m)}) \cdot K^T \nabla_X \partial_z^{n-1-\ell} \tilde{v}_\ell^{(m)}(X, a^{(m)}) \\ &- \tau^{(m)} \sum_{\ell=0}^{n-1} \tilde{F}_{n-1-\ell}^{(m)} (i\alpha) \cdot (K^T \nabla_X \tilde{f}^{(m)}) \partial_z^{n-1-\ell} \tilde{v}_\ell^{(m)}(X, a^{(m)}), \end{aligned} \tag{8}$$

and

$$\tilde{F}_n^{(m)}(X) := \frac{\tilde{f}^{(m)}(X)^n}{n!}, \quad 1 \leq m \leq M.$$

As we mentioned above, the periodic outgoing solutions of (6a) are given by the Rayleigh expansions, c.f. (4),

$$\tilde{v}_n^{(m)}(X, z) = \sum_{p \in \Gamma'} \left\{ d_{n,p}^{(m)} e^{-i\gamma_p^{(m)}(z - a^{(m)})} + u_{n,p}^{(m)} e^{i\gamma_p^{(m)}(z - a^{(m+1)})} \right\} e^{ip \cdot X}, \quad 0 \leq m \leq M,$$

$$d_{n,p}^{(0)} \equiv 0, \quad u_{n,p}^{(M)} \equiv 0, \quad p \in \Gamma'. \tag{9}$$

The boundary conditions (6b) and (6c) allow us to recover the $\{d_{n,p}^{(m)}, u_{n,p}^{(m)}\}$ at each order n and wavenumber p. It is not difficult to see that we must solve

$$\mathbf{A}_p \vec{V}_{n,p} = \vec{R}_{n,p}, \tag{10a}$$

where

$$\vec{V}_{n,p} = \begin{pmatrix} u_{n,p}^{(0)} \\ d_{n,p}^{(1)} \\ u_{n,p}^{(1)} \\ \vdots \\ d_{n,p}^{(M-1)} \\ u_{n,p}^{(M-1)} \\ d_{n,p}^{(M)} \end{pmatrix}, \quad \vec{R}_{n,p} = \begin{pmatrix} \hat{\xi}_{n,p}^{(1)} + \hat{Q}_{n,p}^{(1)} \\ \tau^{(0)} \hat{\nu}_{n,p}^{(1)} + \hat{R}_{n,p}^{(1)} \\ \hat{\xi}_{n,p}^{(2)} + \hat{Q}_{n,p}^{(2)} \\ \vdots \\ \tau^{(M-2)} \hat{\nu}_{n,p}^{(M-1)} + \hat{R}_{n,p}^{(M-1)} \\ \hat{\xi}_{n,p}^{(M)} + \hat{Q}_{n,p}^{(M)} \\ \tau^{(M-1)} \hat{\nu}_{n,p}^{(M)} + \hat{R}_{n,p}^{(M)} \end{pmatrix}, \tag{10b}$$

c.f. (5), which can be solved using Gaussian elimination.

These formulas, (10), completely specify the FE recursions, though we comment on the one complexity, namely the *formation* of the right–hand–sides, $\{\hat{Q}_{n,p}^{(m)}, \hat{R}_{n,p}^{(m)}\}$. This can be effectively specified by examining the first term in $\tilde{Q}_n^{(m)}$, (7),

$$\begin{aligned} \tilde{Q}_n^{(m),1}(X) &= -\sum_{\ell=0}^{n-1} \tilde{F}_{n-\ell}^{(m)}(X) \partial_z^{n-\ell} \tilde{v}_\ell^{(m-1)}(X, a^{(m)}) \\ &= -\sum_{\ell=0}^{n-1} \left(\sum_{p \in \Gamma'} \hat{F}_{n-\ell,p}^{(m)} e^{ip \cdot X} \right) \\ &\quad \times \left(\sum_{q \in \Gamma'} \left[(-i\gamma_q^{(m)})^{n-\ell} \Gamma_q^{(m-1)} d_{\ell,q}^{(m-1)} + (i\gamma_q^{(m)})^{n-\ell} u_{\ell,q}^{(m-1)} \right] e^{iq \cdot X} \right) \\ &= -\sum_{\ell=0}^{n-1} \sum_{p \in \Gamma'} \left(\sum_{q \in \Gamma'} \hat{F}_{n-\ell,p-q}^{(m)} \left[(-i\gamma_q^{(m)})^{n-\ell} \Gamma_q^{(m-1)} d_{\ell,q}^{(m-1)} + (i\gamma_q^{(m)})^{n-\ell} u_{\ell,q}^{(m-1)} \right] \right) e^{ip \cdot X}, \end{aligned}$$

so the Fourier transform of $\tilde{Q}_n^{(m),1}$ can be expressed in terms of the convolution

$$\hat{Q}_{n,p}^{(m),1} = -\sum_{\ell=0}^{n} \sum_{q \in \Gamma'} \hat{F}_{n-\ell,p-q}^{(m)} \left[(-i\gamma_q^{(m)})^{n-\ell} \Gamma_q^{(m-1)} d_{\ell,q}^{(m-1)} + (i\gamma_q^{(m)})^{n-\ell} u_{\ell,q}^{(m-1)} \right]. \tag{11}$$

5. Numerical Results

We have implemented, validated, and explored the capabilities of this new FE method for interfacial shapes which are quasiperiodic. As we shall verify, the spectral character of the Rayleigh expansions and the exponential nature of the Taylor series utilized mandate stunning rates of convergence for the algorithm which make it compelling for many configurations of applied interest. In order to focus, we restricted to the case of one lateral dimensional, $d = 1$, which is lifted to a two–dimensional torus, $D = 2$, implying that $K \in \mathbf{R}^{2 \times 1}$. However, the extension to $d = 2$ and larger D is immediate, though the former would require a consideration of the full Maxwell equations.

5.1. The FE Algorithm

The FE algorithm estimates the Rayleigh–Taylor coefficients $\{d_{n,p}^{(m)}, u_{n,p}^{(m)}\}$ in the expansions (9) for a finite number of perturbation orders, $0 \leq n \leq N$, and a finite subset of wavenumbers,

$$\mathcal{P}(N_X) = \{p \in \Gamma' \mid -N_X^j/2 \leq p_j \leq N_X^j/2 - 1, 1 \leq j \leq 2\}.$$

With these coefficients, the Rayleigh expansions, (9), can be used to recover quantities of interest, e.g., the reflectance and transmittance which we study presently.

To approximate the $\{d_{n,p}^{(m)}, u_{n,p}^{(m)}\}$ we used methods from the family of Spectral Method algorithms [78–81]. More specifically, we approximated functions

$$\tilde{f}(X) \approx \tilde{f}^{N_X}(X) = \sum_{p \in \mathcal{P}(N_X)} \hat{f}_p e^{ip \cdot X},$$

where

$$p = \begin{pmatrix} p_1 \\ p_2 \end{pmatrix}, \quad X = \begin{pmatrix} X_1 \\ X_2 \end{pmatrix}, \quad N_X = \begin{pmatrix} N_X^1 \\ N_X^2 \end{pmatrix}.$$

For smooth functions with periodic derivatives, the $\hat{f}_p$ can be computed with high accuracy via the Trapezoidal Rule. When paired with results on the rapid decay of the Fourier coefficients of such functions, their derivatives can be approximated with high accuracy via

$$\nabla_X \tilde{f}(X) \approx \nabla_X \tilde{f}^{N_X}(X) = \sum_{p \in \mathcal{P}(N_X)} (ip) \hat{f}_p e^{ip \cdot X},$$

as can Fourier multipliers such as

$$(i\gamma_D^{(m)})^\ell \left[\tilde{f}(X)\right] \approx (i\gamma_D^{(m)})^\ell \left[\tilde{f}^{N_X}(X)\right] = \sum_{p \in \mathcal{P}(N_X)} (i\gamma_p^{(m)})^\ell \hat{f}_p e^{ip \cdot X}.$$

We simulated the $\{d_{n,p}^{(m)}, u_{n,p}^{(m)}\}$ by solving (10) at each wavenumber $p \in \mathcal{P}(N_X)$ after forming the right–hand–sides with techniques discussed in regards (11). For this, the derivatives and Fourier multipliers were computed in Fourier space while the convolutions were accomplished with the assistance of the multidimensional FFT algorithm [78–81].

With these coefficients we formed approximations to $\tilde{v}^{(m)}$ by

$$\begin{aligned}\tilde{v}^{(m)}(X, z; \varepsilon) \approx \tilde{v}^{(m),N_x,N}(X, z; \varepsilon) := \sum_{p \in \mathcal{P}(N_X)} &\Big\{ d_p^{(m),N}(\varepsilon) e^{-i\gamma_p^{(m)}(z - a^{(m)})} \\ &+ u_p^{(m),N}(\varepsilon) e^{i\gamma_p^{(m)}(z - a^{(m+1)})} \Big\} e^{ip \cdot X},\end{aligned}$$

where

$$d_p^{(m),N}(\varepsilon) := \sum_{n=0}^{N} d_{n,p}^{(m)} \varepsilon^n, \quad u_p^{(m),N}(\varepsilon) := \sum_{n=0}^{N} u_{n,p}^{(m)} \varepsilon^n, \tag{12}$$

and the question arises: How are the truncated Taylor series in (12) to be summed? As we have observed [47, 49, 82], Padé summation can be coupled to HOPS algorithms with great success and we utilized it here. Padé approximation estimates the truncated Taylor series in (12) by the rational function

$$[L/M](\varepsilon) := \frac{A^L(\varepsilon)}{B^M(\varepsilon)} = \frac{\sum_{\ell=0}^{L} A_\ell \varepsilon^\ell}{1 + \sum_{m=1}^{M} B_m \varepsilon^m}, \quad L + M = N,$$

and

$$[L/M](\varepsilon) = d_p^{(m),N}(\varepsilon) + O(\varepsilon^{L+M+1}).$$

Classical formulas for the $\{A_\ell, B_m\}$ are described in [59] and these approximants have noteworthy properties of enhanced convergence and analytic continuation. We refer the interested reader to § 2.2 of Baker & Graves–Morris [59] and the explicit calculations in § 8.3 of Bender & Orszag [83] for a complete discussion of capabilities and limitations.

5.2. *Validation*

We used the Method of Manufactured Solutions (MMS) [84–86] to validate our implementation. This scheme uses the observation that, in devising a solver for a generic system of partial differential equations and boundary conditions

$$\begin{aligned} \mathcal{P}v &= 0, && \text{in } \Omega, \\ \mathcal{B}v &= 0, && \text{at } \partial\Omega, \end{aligned}$$

it is often just as easy to construct one for the corresponding inhomogeneous problem

$$\begin{aligned} \mathcal{P}v &= \mathcal{R}, && \text{in } \Omega, \\ \mathcal{B}v &= \mathcal{J}, && \text{at } \partial\Omega. \end{aligned}$$

To test a code one can select a "manufactured solution," v', and choose

$$\mathcal{R}' = \mathcal{P}v', \quad \mathcal{J}' = \mathcal{B}v'.$$

Now, associated to the pair $\{\mathcal{R}', \mathcal{J}'\}$ we have the *exact* solution of the latter problem, v', against which to measure errors. While this test is not foolproof, if v' is chosen to have behavior similar to desired solutions (e.g., exactly satisfying boundary conditions), then this can give us great confidence in our implementation.

In the current context we considered the functions

$$\tilde{v}^{(0),\text{exact}}(X,z) := A_r e^{ir\cdot X + i\gamma_r^{(0)}(z-a^{(1)})}, \quad \tilde{v}^{(M),\text{exact}}(X,z) := D_r e^{ir\cdot X - i\gamma_r^{(M)}(z-a^{(M)})},$$
$$\tilde{v}^{(m),\text{exact}}(X,z) := B_r^{(m)} e^{ir\cdot X - i\gamma_r^{(m)}(z-a^{(m)})} + C_r^{(m)} e^{ir\cdot X + i\gamma_r^{(m)}(z-a^{(m+1)})}, \quad 1 \le m \le M-1,$$

for $r \in \mathbf{Z}^2$, which are Γ–periodic solutions of the Helmholtz equations (3), and outgoing in $S^{(0)}$ and $S^{(M)}$. With these we defined the Dirichlet and Neumann interfacial traces

$$\begin{aligned} \tilde{V}^{(m),u,\text{exact}}(X) &:= \left[\tilde{v}^{(m),\text{exact}}\right]_{z=a^{(m)}+\tilde{g}^{(m)}(X)}, && 1 \le m \le M, \\ \tilde{V}^{(m),\ell,\text{exact}}(X) &:= \left[\tilde{v}^{(m),\text{exact}}\right]_{z=a^{(m+1)}+\tilde{g}^{(m+1)}(X)}, && 0 \le m \le M-1, \\ \tilde{V}'^{,(m),u,\text{exact}}(X) &:= \left[\tilde{\mathcal{N}}^{(m)}\tilde{v}^{(m),\text{exact}}\right]_{z=a^{(m)}+\tilde{g}^{(m)}(X)}, && 1 \le m \le M, \\ \tilde{V}'^{,(m),\ell,\text{exact}}(X) &:= \left[\tilde{\mathcal{N}}^{(m)}\tilde{v}^{(m),\text{exact}}\right]_{z=a^{(m+1)}+\tilde{g}^{(m+1)}(X)}, && 0 \le m \le M-1. \end{aligned}$$

We selected TM polarization, $M = 5$ interfaces ($M + 1 = 6$ layers), physical parameters

$$a^{(m)} \in \{1.5, 0.775, 0.05, -0.675, -1.4\}, \quad \epsilon^{(m)} \in \{1.1, 1.14, 1.18, 1.22, 1.26, 1.3\},$$
$$\lambda = 2\pi, \quad \theta = 30^\circ, \quad K = (1,\kappa)^T, \quad \kappa = \sqrt{2}, \tag{13}$$

and numerical parameters

$$N_X^1 = N_X^2 = 16, \quad N = 16. \tag{14}$$

To study our implementation we chose the layer deformations

$$\tilde{g}^{(m)}(X) = \varepsilon \tilde{f}^{(m)}(X), \quad \tilde{f}^{(m)}(X) = \begin{cases} \sin(X_1)\sin(X_2), & m = 1, \\ \cos(X_1)\cos(X_2), & m = 2, \\ \sin(X_1)\cos(X_2), & m = 3, \\ \cos(X_1)\sin(X_2), & m = 4, \\ \sin(X_1)\sin(X_2), & m = 5, \end{cases}$$

three values of ε,

$$\varepsilon = 0.02, 0.1, 0.25,$$

and MMS parameters

$$\begin{aligned} r = (1,1)^T, \quad A_r = -3, \quad D_r = -e, \\ B_r^{(m)} \in \{\pi, 2\pi, 3\pi, 4\pi\}, \quad C_r^{(m)} \in \{4, 2, 0, -2\}. \end{aligned} \tag{15}$$

With these choices, we set

$$\begin{aligned} \tilde{\xi}^{(m)} &= \tilde{V}^{(m-1),\ell,\text{exact}} - \tilde{V}^{(m),u,\text{exact}}, & 1 \le m \le M, \\ \tau^{(m-1)}\tilde{\nu}^{(m)} &= \tau^{(m-1)}\tilde{V}^{\prime,(m-1),\ell,\text{exact}} - \tau^{(m)}\tilde{V}^{\prime,(m),u,\text{exact}}, & 1 \le m \le M, \end{aligned}$$

and sent these to our implementation which delivered approximations to the $\{u_{n,p}^{(m)}, d_{n,p}^{(m)}\}$ that we subsequently used to compute the estimates $\tilde{V}^{(0),\ell,\text{approx}}$ and $\tilde{V}^{\prime,(0),\ell,\text{approx}}$. (The results were similar for $\tilde{V}^{(m),\ell/u,\text{approx}}$ and $\tilde{V}^{\prime,(m),\ell/u,\text{approx}}$, $m > 0$.) With these we computed the relative errors, e.g.,

$$\text{Error}_{\text{rel}} = \frac{\left|\tilde{V}^{(0),\ell,\text{approx}} - \tilde{V}^{(0),\ell,\text{exact}}\right|_{L^\infty}}{\left|\tilde{V}^{(0),\ell,\text{exact}}\right|_{L^\infty}}. \tag{16}$$

In Figure 3 we depict the results of this simulation for a small choice of the perturbation parameter, $\varepsilon = 0.02$. This shows the extremely rapid and robust convergence of our method using either Taylor or Padé summation for the upper traces $\{\tilde{V}^{(0),\ell}, \tilde{V}^{\prime,(0),\ell}\}$. In fact, since the vertical axis is logarithmic we conclude that the rate of convergence is spectral and we effectively achieve machine precision after merely $N = 6$ perturbation orders.

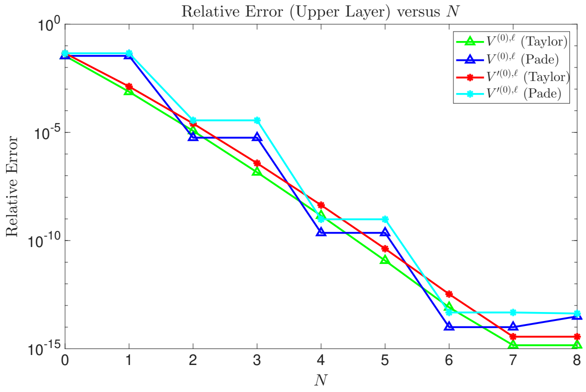

Fig. 3. Plot of relative error, (16), for a small perturbation ($\varepsilon = 0.02$) in the interfacial data $\{\tilde{V}^{(0),\ell}, \tilde{V}^{\prime,(0),\ell}\}$ using both Taylor and Padé summation. Physical parameters were (13), numerical discretization was (14), and MMS values were (15).

Figure 4 displays the results of our experiments for a moderate choice of the perturbation parameter, $\varepsilon = 0.1$. While requiring more perturbation orders, we note once again the rapid and steady convergence of our method using either Taylor or Padé summation. Again, we notice a spectral rate of convergence down to machine precision, though it now requires 10–12 perturbation orders.

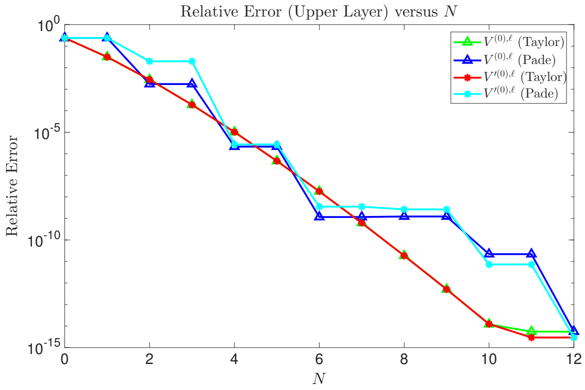

Fig. 4. Plot of relative error, (16), for a medium perturbation ($\varepsilon = 0.1$) in the interfacial data $\{\tilde{V}^{(0),\ell}, \tilde{V}'^{,(0),\ell}\}$ using both Taylor and Padé summation. Physical parameters were (13), numerical discretization was (14), and MMS values were (15).

We finish our discussion with Figure 5 which catalogues our findings for a large choice of the perturbation parameter, $\varepsilon = 0.25$. As above, we see rapid and steady convergence of our method using either Taylor or Padé summation. As with the previous two simulations, we see spectral convergence of our numerical method, though now requiring 12–16 perturbation orders to realize machine precision.

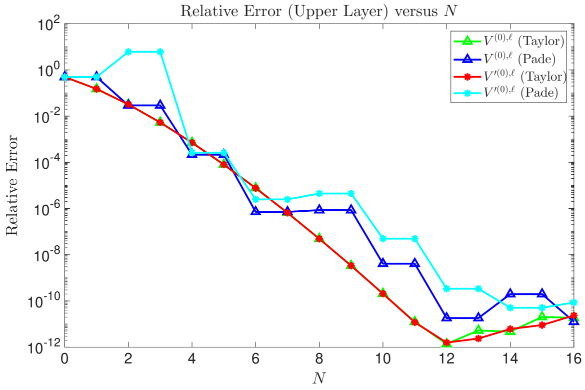

Fig. 5. Plot of relative error, (16), for a large perturbation ($\varepsilon = 0.25$) in the interfacial data $\{\tilde{V}^{(0),\ell}, \tilde{V}'^{,(0),\ell}\}$ using both Taylor and Padé summation. Physical parameters were (13), numerical discretization was (14), and MMS values were (15).

5.3. Three–Layer Nonlinear Dispersion Relations

With the veracity of our implementation established, we chose, as in [73], to revisit computations from the plasmonics literature [3–5] with this new capability of simulating multilayered quasiperiodic gratings. More specifically, we studied the "nonlinear dispersion relation" of surface plasmons which are induced by the weakly nonlinear effect of time–harmonic incident radiation, propagating in vacuum, interacting with small interfacial deformations in the interfaces of layers of silver and vacuum. (The classical linear dispersion relation involves the propagation of a waveform with a *single* wavenumber [3] in contrast to the configuration we discuss here where *all* wavenumbers are excited, though most are quite small [74].)

The linear dispersion relation satisfied by time–harmonic (frequency ω), spatially periodic (wavenumber q) electromagnetic plane waves propagating in vacuum is a classical relation [87] given by

$$q = \frac{\omega}{c_0}.$$

This will be seen in future plots and discussed as the "light line." In a similar vein, time–harmonic, normally incident ($\theta = 0°$), spatially periodic surface plasmons at a single dielectric–metal interface (vacuum–silver in this paper) must obey [3]

$$q = \frac{\omega}{c_0}\sqrt{\frac{\epsilon^{(0)}\epsilon^{(1)}}{\epsilon^{(0)} + \epsilon^{(1)}}}, \quad \epsilon^{(1)} = \epsilon^{(1)}(\omega), \tag{17}$$

though, one usually considers the real part of $\epsilon^{(1)}(\omega)$ in order to make meaningful plots. It is this SPR dispersion relation which we attempted to reproduce in the multilayer case. However, this useful formula is only true in the double–layer case and there is no, straightforward, multi–layer analogue. In the absence of this, we computed the (logarithm of the) condition number of the matrix $\mathbf{A}_p$, c.f. (5), as singularities of this for a given wavenumber $p \in \Gamma'$ indicate the dispersion relation of SPRs. Our simulations of the absorbance of assorted multi–layer structures will be compared with plots of this measure of matrix singularity.

In order to simulate the dispersion relation of SPRs for multilayered structures we selected sinusoidal profiles

$$\begin{gathered} g_m(x) = \varepsilon f_m(x), \quad f_m(x) = \tilde{f}^{(m)}(Kx), \quad K = \frac{2\pi}{d}(1,\kappa)^T, \\ \tilde{f}^{(m)}(X) = b_m \cos(X_1) + c_m \cos(X_2), \end{gathered} \tag{18}$$

and chose $\varepsilon = 0.002$ in order to excite a surface plasmon; it is well–known that a single *flat* interface cannot generate an SPR [3].

We began with a two–interface ($M = 2$), three–layer ($M+1 = 3$) configuration with $b_1 = b_2 = 1$ and $c_1 = c_2 = 0$, which corresponds to the classical excitation of an SPR by commensurate sinusoids [3]. We focused on TM polarization, chose physical parameters

$$\begin{gathered} \epsilon^{(0)} = \epsilon^{(2)} = 1, \quad \epsilon^{(1)} = \epsilon^{\mathrm{Ag}}(\omega), \\ 0.400\,\mu m \leq d \leq 2.000\,\mu m, \qquad 0.800\,\mu m \leq \lambda \leq 2.000\,\mu m, \end{gathered} \tag{19}$$

from which we computed

$$q = 2\pi/d, \quad \omega = 2\pi c_0/\lambda,$$

and numerical parameters

$$N_X^1 = N_X^2 = 16, \quad N = 16. \tag{20}$$

In Figure 6 (upper left) we show results of our simulations which displays the absorbance of our structure, $A = 1 - R - T$, where R and T are the reflectance and transmittance [76], respectively, as a function of the wavenumber of the interface and frequency of illumination. We view a spike in absorbance as an indicator of an SPR as this means that the incident energy is neither reflected nor transmitted, but rather propagating along the insulator–metal interfaces. Here we see ridges of values in the range 0.2–0.25 in an ocean of quite small (less than 0.05) values. This is to be

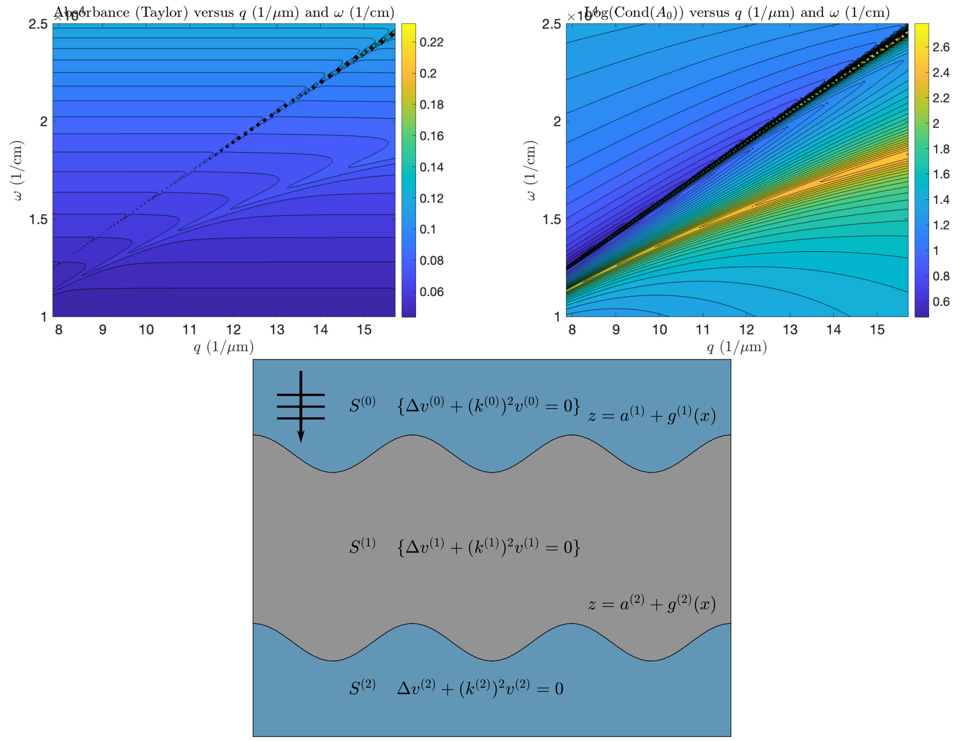

Fig. 6. (Above, left): Contour plot of absorbance as a function of wavenumber, q (inverse microns), and illumination frequency, ω (inverse centimeters), for a triply layered vacuum–silver structure with sinusoidal interfaces ($b_1 = b_2 = 1, c_1 = c_2 = 0$), (18), of amplitude $\varepsilon = 0.002$ using Taylor summation. Physical parameters were (19) and numerical discretization was (20). (Above, right): Contour plot of the logarithm of the condition number of $\mathbf{A}_p$ which measures the singularity in $\mathbf{A}_p$ and the dispersion relation for this configuration. (Below): Plot of the grating structure.

compared with Figure 6 (upper right) which shows the linear dispersion relation (measured by the condition number of $\mathbf{A}_p$ as a function of q and ω) and see quite close qualitative agreement. This gives us confidence that our code can reproduce this classic result.

We then moved to a much more challenging periodic configuration which our new formulation can handle with ease. Here the interfaces are have two, widely disparate, periods: d and rd, $r \in \mathbf{Z}$. We made this more specific by choosing the deformations $\tilde{f}^{(m)}$, (18), with $b_1 = 1$, $b_2 = 0$, $c_1 = 0$, $c_2 = 1$, and both (i.) $\kappa = 1 + 1/r$, giving

$$f^{(1)}(x) = \cos\left(\frac{2\pi x}{d}\right), \quad f^{(2)}(x) = f_+(x) = \cos\left(\frac{2\pi(r+1)x}{rd}\right),$$

and (ii.) $\kappa = 1 - 1/r$, resulting in

$$f^{(1)}(x) = \cos\left(\frac{2\pi x}{d}\right), \quad f^{(2)}(x) = f_-(x) = \cos\left(\frac{2\pi(r-1)x}{rd}\right).$$

The former constitutes a *superharmonic* (period shorter than the base period) perturbation and the latter a *subharmonic* (period longer than the base) deviation. We found these to be interesting computations as simulations based upon a *periodic* implementation [40] would require (rN_X^1) unknowns for the same spatial accuracy that our code delivers. Clearly, if $r > N_X^1$ our method will enjoy smaller memory requirements and computational complexity, setting aside the issue that numerical methods for PDE typically have deteriorating conditioning properties as the number of spatial discretization points increases [80, 88, 89].

In Figures 7 and 8 we depict contour plots of absorbance versus wavenumber and frequency in the case $r = 4$ for superharmonic and subharmonic perturbations, respectively. In contrast to our previous results, we now see *four* pronounced ridges of larger absorbance values, each of which can be identified with ridges in the linear dispersion relation shown in the upper right of each figure. This shows that our implementation can quickly, efficiently, and accurately predict the SPRs which this structure excites.

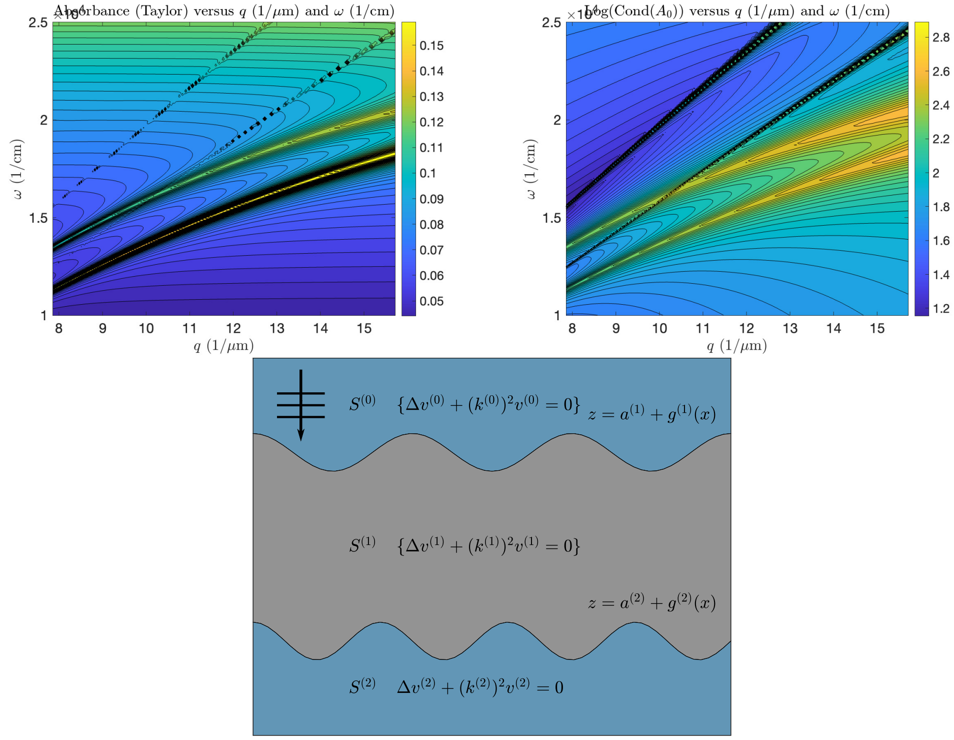

Fig. 7. (Above, left): Contour plot of absorbance as a function of wavenumber, q (inverse microns), and illumination frequency, ω (inverse centimeters), for a triply layered vacuum–silver structure with sinusoidal interfaces ($b_1 = 1$, $b_2 = 0$, $c_1 = 0$, $c_2 = 1$, $\kappa = 1 + 1/4$, $r = 4$), (18), of amplitude $\varepsilon = 0.002$ using Taylor summation. Physical parameters were (19) and numerical discretization was (20). (Above, right): Contour plot of the logarithm of the condition number of $\mathbf{A}_p$ which measures the singularity in $\mathbf{A}_p$ and the dispersion relation for this configuration. (Below): Plot of the grating structure.

We reprised these computations in the more challenging case $r = 64$ which features interfaces with periods d and $64d$. In this case if one is satisfied with, say, 16 gridpoints per period then a periodic HOPS scheme mandates $N_x = 64 \times 16 = 1024$ while our new scheme only requires $N_X^1 \times N_X^2 = 16 \times 16 = 256$, a factor of four smaller. In Figures 9 and 10 we display contour plots of absorbance versus wavenumber and frequency in this case $r = 64$ for superharmonic and subharmonic perturbations, respectively. While more difficult to see due to the closeness of the SPR dispersion relations when the wavenumber changes so slightly, this shows our implementation to be a rapid and robust method for realizing *all* of these.

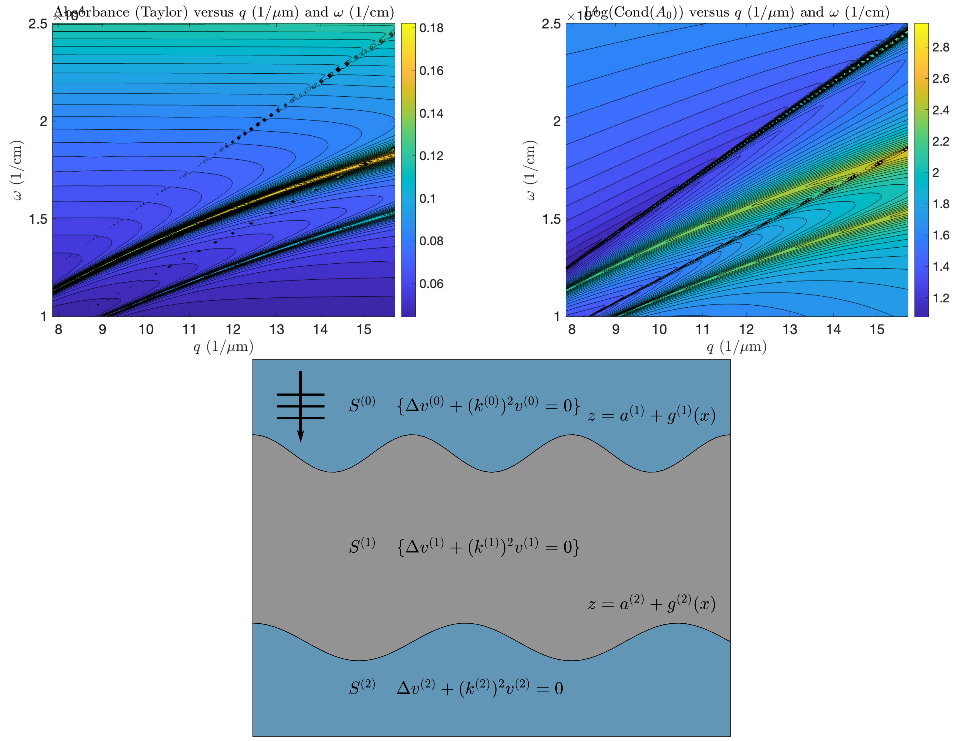

Fig. 8. (Above, left): Contour plot of absorbance as a function of wavenumber, q (inverse microns), and illumination frequency, ω (inverse centimeters), for a triply layered vacuum–silver structure with sinusoidal interfaces ($b_1 = 1$, $b_2 = 0$, $c_1 = 0$, $c_2 = 1$, $\kappa = 1 - 1/4$, $r = 4$), (18), of amplitude $\varepsilon = 0.002$ using Taylor summation. Physical parameters were (19) and numerical discretization was (20). (Above, right): Contour plot of the logarithm of the condition number of $\mathbf{A}_p$ which measures the singularity in $\mathbf{A}_p$ and the dispersion relation for this configuration. (Below): Plot of the grating structure.

To finish the discussion of our three–layer numerical experiments we chose a configuration which is *beyond* a periodic implementation, but which our new algorithm handles seamlessly. To demonstrate this we chose, in the deformations $\tilde{f}^{(m)}$, (18), with $b_1 = 1$, $b_2 = 0$, $c_1 = 0$, $c_2 = 1$, with both $\kappa = \sqrt{2}$ (superharmonic) and $\kappa = 1/\sqrt{2}$ (subharmonic) perturbations. In Figures 11 and 12 we show absorbance versus wavenumber and frequency, and we notice ridges of larger values which precisely match the dispersion relation depicted in the upper right. With this we have an accurate and rapid prediction of SPR dispersion relations for a configuration which is *impossible* for other algorithms to approximate.

5.4. Five–Layer Nonlinear Dispersion Relations

Having thoroughly investigated the case of $M = 2$ interfaces ($M + 1 = 3$ layers) we moved with ease to the case of $M = 4$ interfaces ($M + 1 = 5$ layers) with, once again, the goal of reproducing the SPR dispersion relation for these more complex diffraction gratings. While we considered more layers, the spirit of the structure remains alternate layers of vacuum and silver. We began with $M = 4$ and

$$b_1 = b_2 = b_3 = b_4 = 1, \quad c_1 = c_2 = c_3 = c_4 = 0,$$

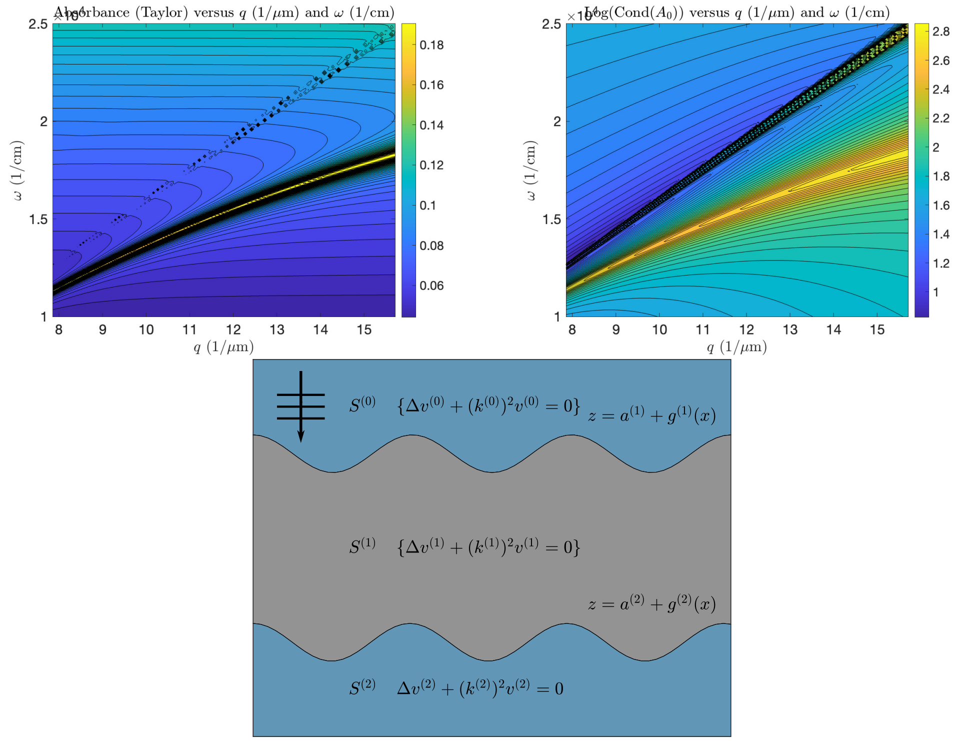

Fig. 9. (Above, left): Contour plot of absorbance as a function of wavenumber, q (inverse microns), and illumination frequency, ω (inverse centimeters), for a triply layered vacuum–silver structure with sinusoidal interfaces ($b_1 = 1$, $b_2 = 0$, $c_1 = 0$, $c_2 = 1$, $\kappa = 1 + 1/64$, $r = 64$), (18), of amplitude $\varepsilon = 0.002$ using Taylor summation. Physical parameters were (19) and numerical discretization was (20). (Above, right): Contour plot of the logarithm of the condition number of $\mathbf{A}_p$ which measures the singularity in $\mathbf{A}_p$ and the dispersion relation for this configuration. (Below): Plot of the grating structure.

which corresponds to the excitation of an SPR by commensurate sinusoids [3], focused on TM polarization, chose physical parameters (19), and numerical parameters (20).

In Figure 13 we show results of our simulations which displays the absorbance of our structure as a function of the wavenumber of the interface and frequency of illumination. Here we see a ridge of large values reproduced by the dispersion relation described by the singularities of $\mathbf{A}_p$.

As before, we then moved to more difficult periodic configurations featuring the profiles f_+ and f_- above. More specifically we chose the deformations $\tilde{f}^{(m)}$, (18), with

$$b_1 = 1, b_2 = 0, b_3 = 1, b_4 = 0, \quad c_1 = 0, c_2 = 1, c_3 = 0, c_4 = 1,$$

and both (i.) $\kappa = 1 + 1/r$, giving

$$f^{(1)}(x) = f^{(3)}(x) = \cos\left(\frac{2\pi x}{d}\right), \quad f^{(2)}(x) = f^{(4)}(x) = f_+(x) = \cos\left(\frac{2\pi(r+1)x}{rd}\right),$$

and (ii.) $\kappa = 1 - 1/r$, resulting in

$$f^{(1)}(x) = f^{(3)}(x) = \cos\left(\frac{2\pi x}{d}\right), \quad f^{(2)}(x) = f^{(4)}(x) = f_-(x) = \cos\left(\frac{2\pi(r-1)x}{rd}\right).$$

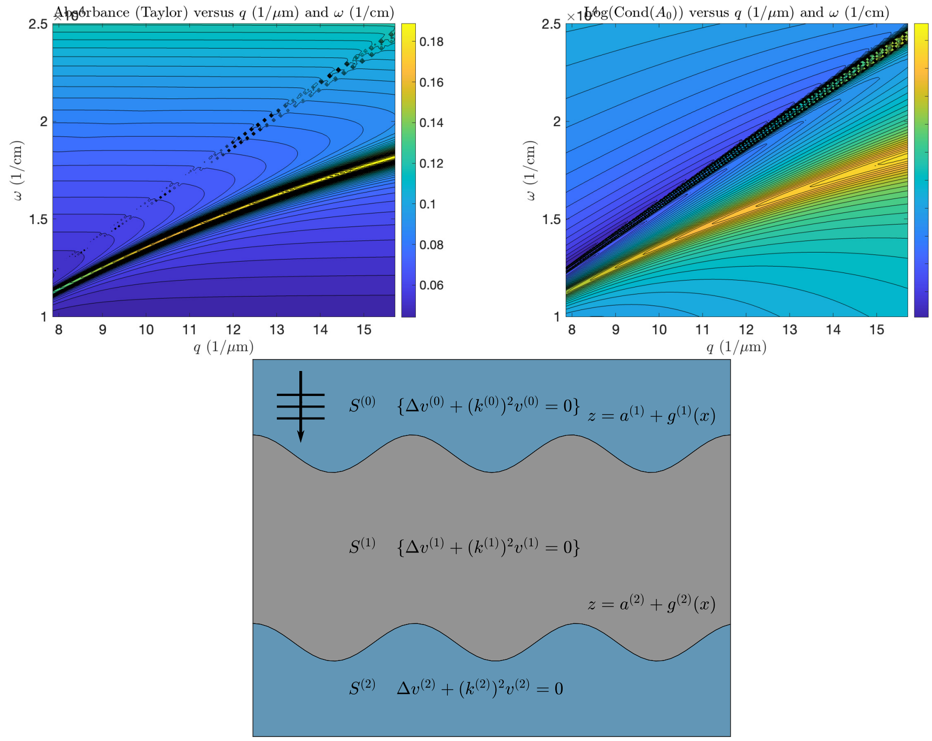

Fig. 10. (Above, left): Contour plot of absorbance as a function of wavenumber, q (inverse microns), and illumination frequency, ω (inverse centimeters), for a triply layered vacuum–silver structure with sinusoidal interfaces ($b_1 = 1$, $b_2 = 0$, $c_1 = 0$, $c_2 = 1$, $\kappa = 1 - 1/64$, $r = 64$), (18), of amplitude $\varepsilon = 0.002$ using Taylor summation. Physical parameters were (19) and numerical discretization was (20). (Above, right): Contour plot of the logarithm of the condition number of $\mathbf{A}_p$ which measures the singularity in $\mathbf{A}_p$ and the dispersion relation for this configuration. (Below): Plot of the grating structure.

As before, we term the former a *superharmonic* perturbation and the latter a *subharmonic* deviation.

In Figures 14 and 15 we show contour plots of absorbance versus wavenumber and frequency in the case $r = 4$ for superharmonic and subharmonic perturbations, respectively. As before, we see *several* pronounced ridges of larger absorbance values, each of which can be identified with structures in the plots of the dispersion relation characterized by singularities in $\mathbf{A}_p$. This shows that our implementation can quickly, efficiently, and accurately predict the SPRs which these gratings excite.

We revisited these computations in the challenging case $r = 64$ which features interfaces with periods d and $64d$. In Figures 16 and 17 we display contour plots of absorbance versus wavenumber and frequency in this case $r = 64$ for superharmonic and subharmonic perturbations, respectively. While more difficult to see due to the closeness of the SPR dispersion relations when the wavenumber changes so slightly, this shows our implementation to be a rapid and robust method for realizing *all* of these.

To complete the discussion of our five–layer numerical experiments we chose a configuration which is, as before, *impossible* for a periodic implementation, but which our new algorithm

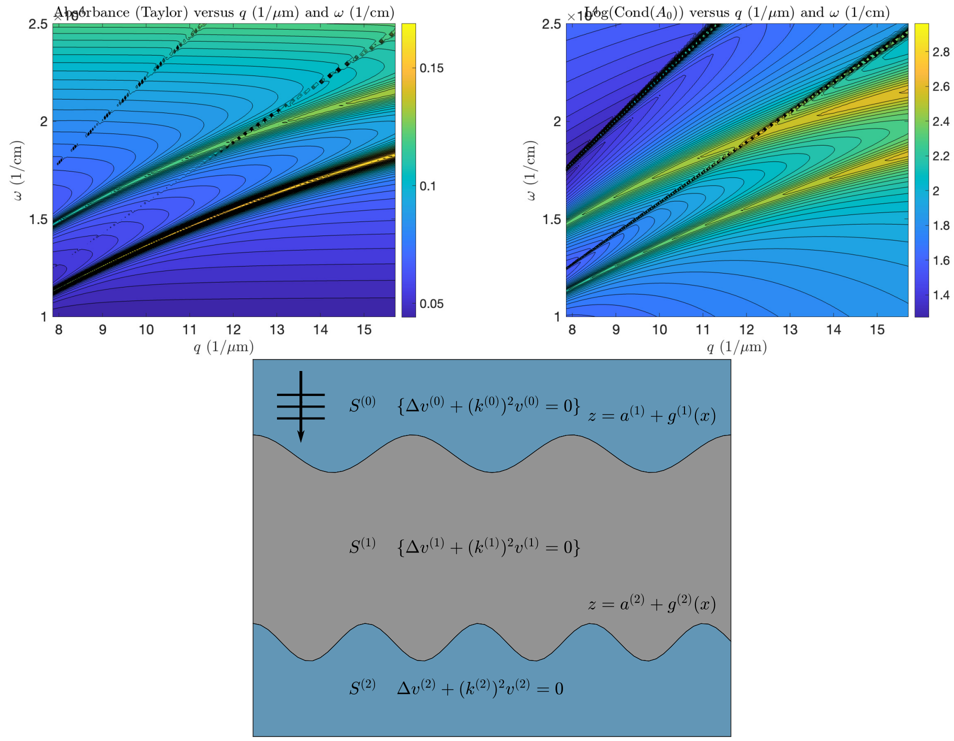

Fig. 11. (Above, left): Contour plot of absorbance as a function of wavenumber, q (inverse microns), and illumination frequency, ω (inverse centimeters), for a triply layered vacuum–silver structure with sinusoidal interfaces ($b_1 = 1$, $b_2 = 0$, $c_1 = 0$, $c_2 = 1$, $\kappa = 1 + \sqrt{2}$), (18), of amplitude $\varepsilon = 0.002$ using Taylor summation. Physical parameters were (19) and numerical discretization was (20). (Above, right): Contour plot of the logarithm of the condition number of $\mathbf{A}_p$ which measures the singularity in $\mathbf{A}_p$ and the dispersion relation for this configuration. (Below): Plot of the grating structure.

handles without issue. For this we chose, in the deformations $\tilde{f}^{(m)}$, (18),

$$b_1 = 1, b_2 = 0, b_3 = 1, b_4 = 0, \quad c_1 = 0, c_2 = 1, c_3 = 0, c_4 = 1,$$

with both $\kappa = \sqrt{2}$ (superharmonic) and $\kappa = 1/\sqrt{2}$ (subharmonic) perturbations. In Figures 18 and 19 we show absorbance versus wavenumber and frequency, and we notice the ridges of larger values which match the singularities of $\mathbf{A}_p$ with excellent qualitative precision.

6. Concluding Remarks and Future Directions

In this paper the author has derived a new HOPS scheme for the numerical simulation of scattering returns by multiply–layered media with a quasiperiodic interfaces. The algorithm was implemented and verified, and then used it to simulate nonlinear dispersion relations for layered vacuum–silver structures with quasiperiodic interfaces. The scheme was shown to be rapid, robust, and reliable and able to address configurations impossible for standard algorithms. There are many possible future directions for this work and the author plans to investigate several of these. Paramount is the generalization of this approach to the fully vectorial three dimensional Maxwell equations.

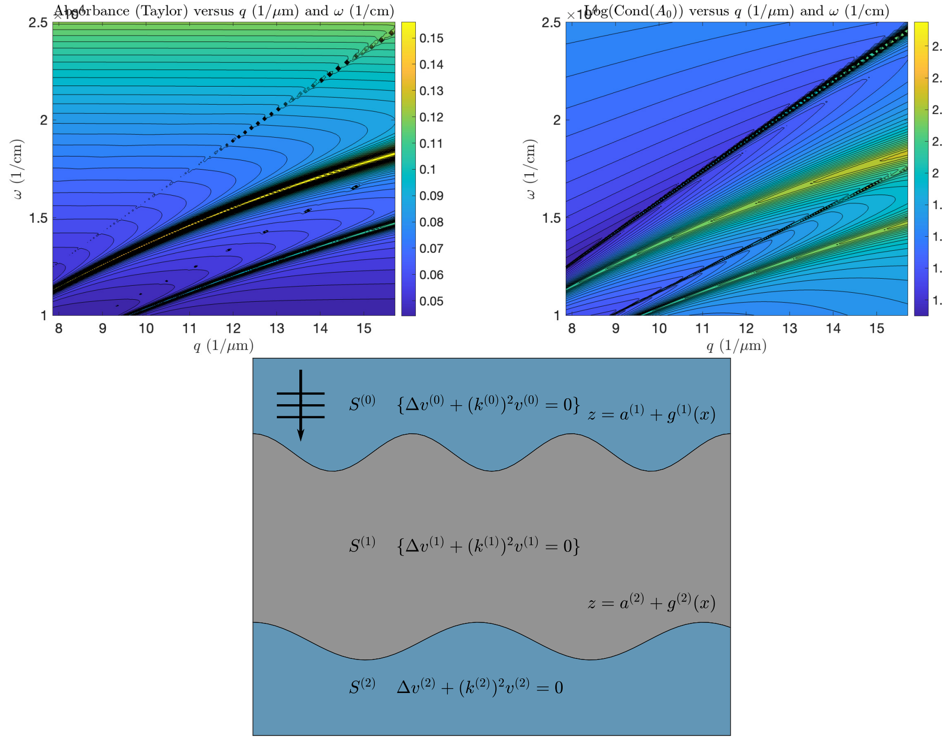

Fig. 12. (Above, left): Contour plot of absorbance as a function of wavenumber, q (inverse microns), and illumination frequency, ω (inverse centimeters), for a triply layered vacuum–silver structure with sinusoidal interfaces ($b_1 = 1$, $b_2 = 0$, $c_1 = 0$, $c_2 = 1$, $\kappa = 1 - \sqrt{2}$), (18), of amplitude $\varepsilon = 0.002$ using Taylor summation. Physical parameters were (19) and numerical discretization was (20). (Above, right): Contour plot of the logarithm of the condition number of $\mathbf{A}_p$ which measures the singularity in $\mathbf{A}_p$ and the dispersion relation for this configuration. (Below): Plot of the grating structure.

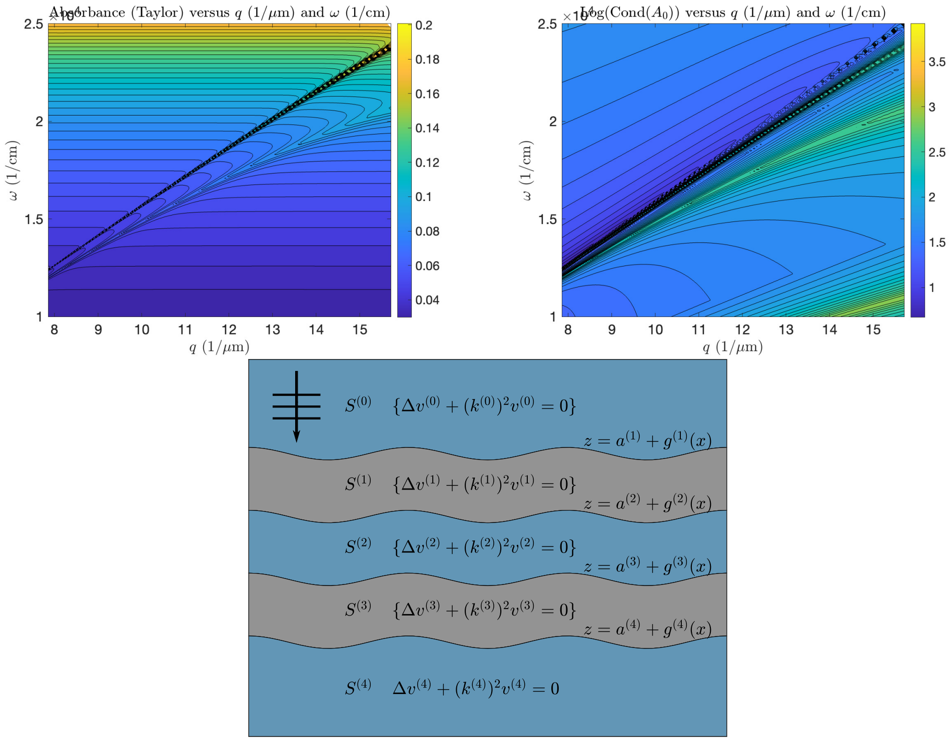

Fig. 13. (Above, left): Contour plot of absorbance as a function of wavenumber, q (inverse microns), and illumination frequency, ω (inverse centimeters), for a quintuply layered vacuum–silver structure with sinusoidal interfaces ($b_1 = b_2 = b_3 = b_4 = 1, c_1 = c_2 = c_3 = c_4 = 0$), (18), of amplitude $\varepsilon = 0.002$ using Taylor summation. Physical parameters were (19) and numerical discretization was (20). (Above, right): Contour plot of the logarithm of the condition number of $\mathbf{A}_p$ which measures the singularity in $\mathbf{A}_p$ and the dispersion relation for this configuration. (Below): Plot of the grating structure.

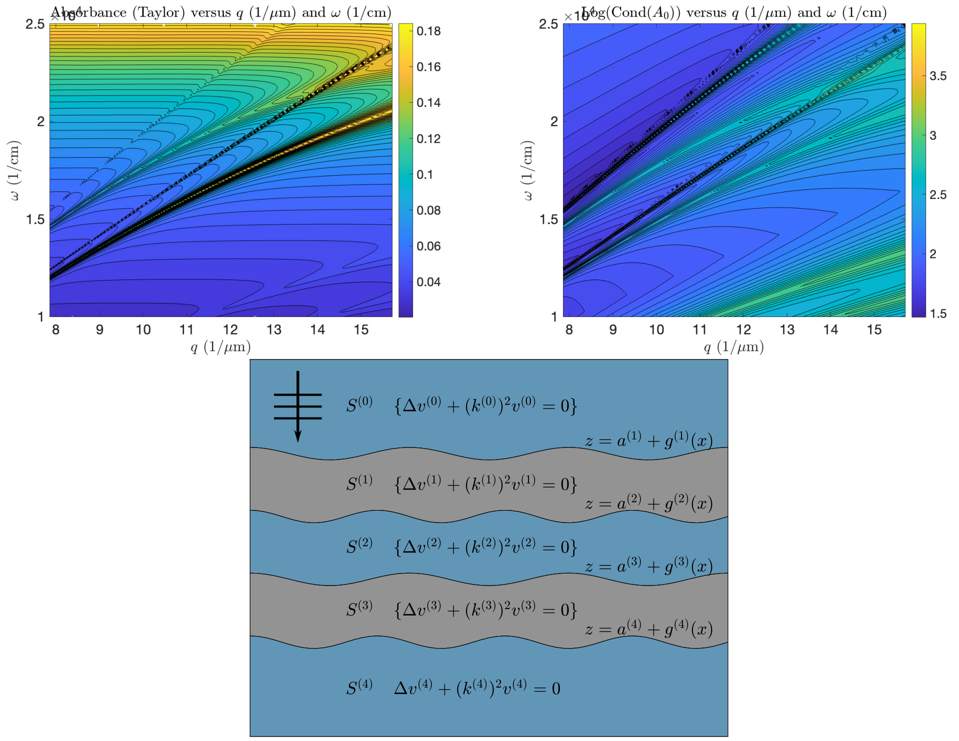

Fig. 14. (Above, left): Contour plot of absorbance as a function of wavenumber, q (inverse microns), and illumination frequency, ω (inverse centimeters), for a quintuply layered vacuum–silver structure with sinusoidal interfaces ($b_1 = b_3 = 1$, $b_2 = b_4 = 0$, $c_1 = c_3 = 0$, $c_2 = c_4 = 1$, $\kappa = 1 + 1/4$, $r = 4$), (18), of amplitude $\varepsilon = 0.002$ using Taylor summation. Physical parameters were (19) and numerical discretization was (20). (Above, right): Contour plot of the logarithm of the condition number of $\mathbf{A}_p$ which measures the singularity in $\mathbf{A}_p$ and the dispersion relation for this configuration. (Below): Plot of the grating structure.

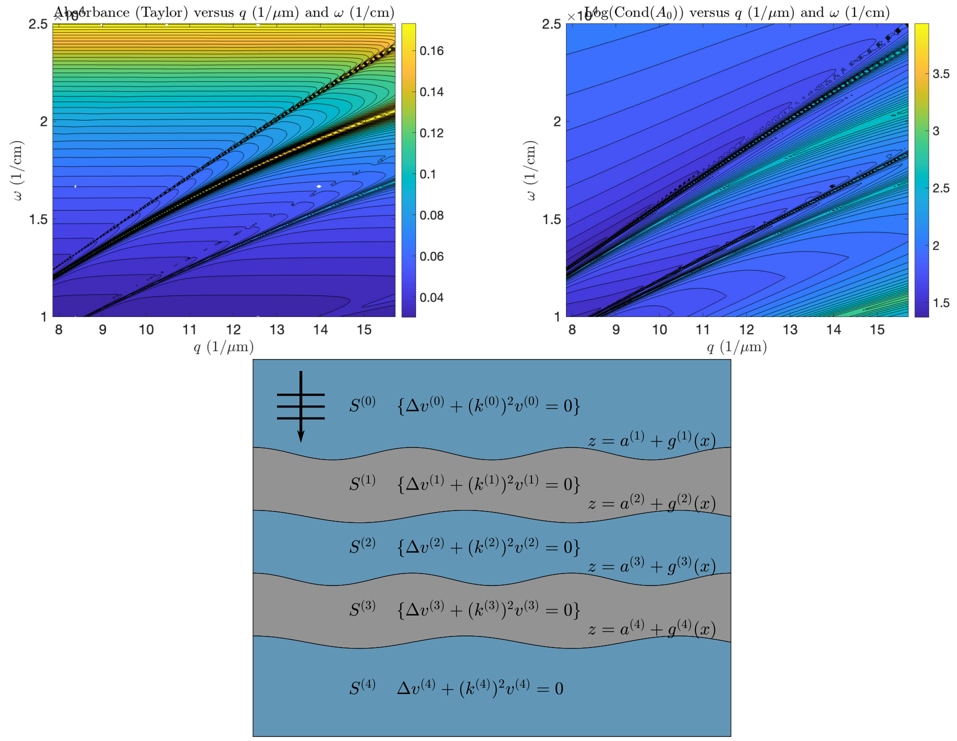

Fig. 15. (Above, left): Contour plot of absorbance as a function of wavenumber, q (inverse microns), and illumination frequency, ω (inverse centimeters), for a quintuply layered vacuum–silver structure with sinusoidal interfaces ($b_1 = b_3 = 1$, $b_2 = b_4 = 0$, $c_1 = c_3 = 0$, $c_2 = c_4 = 1$, $\kappa = 1 - 1/4$, $r = 4$), (18), of amplitude $\varepsilon = 0.002$ using Taylor summation. Physical parameters were (19) and numerical discretization was (20). (Above, right): Contour plot of the logarithm of the condition number of $\mathbf{A}_p$ which measures the singularity in $\mathbf{A}_p$ and the dispersion relation for this configuration. (Below): Plot of the grating structure.

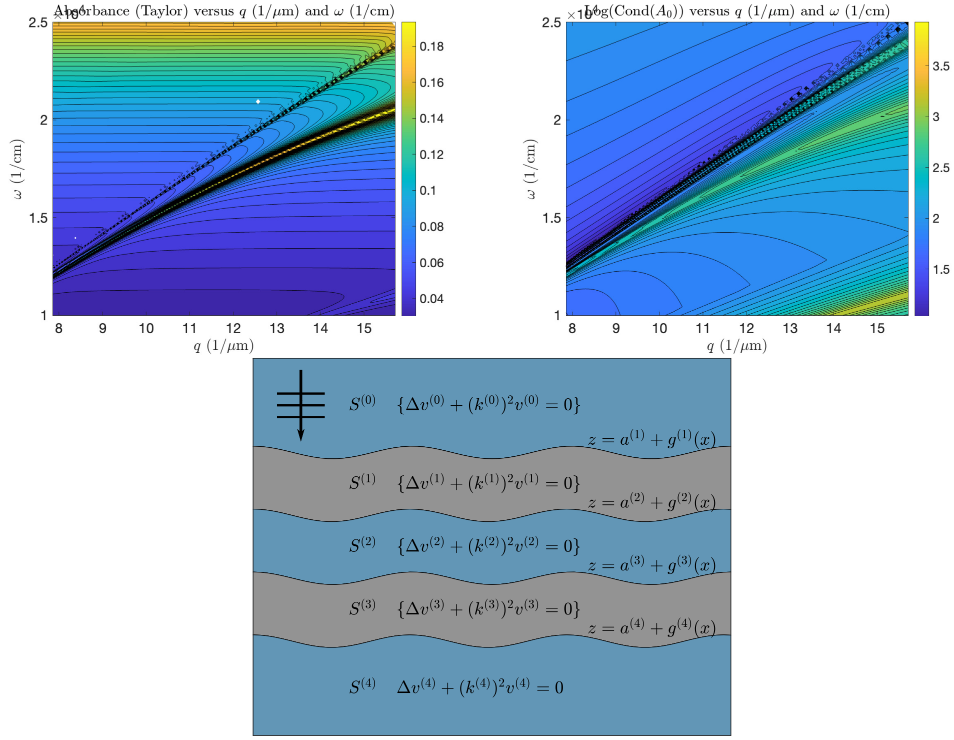

Fig. 16. (Above, left): Contour plot of absorbance as a function of wavenumber, q (inverse microns), and illumination frequency, ω (inverse centimeters), for a quintuply layered vacuum–silver structure with sinusoidal interfaces ($b_1 = b_3 = 1$, $b_2 = b_4 = 0$, $c_1 = c_3 = 0$, $c_2 = c_4 = 1$, $\kappa = 1 + 1/64$, $r = 64$), (18), of amplitude $\varepsilon = 0.002$ using Taylor summation. Physical parameters were (19) and numerical discretization was (20). (Above, right): Contour plot of the logarithm of the condition number of $\mathbf{A}_p$ which measures the singularity in $\mathbf{A}_p$ and the dispersion relation for this configuration. (Below): Plot of the grating structure.

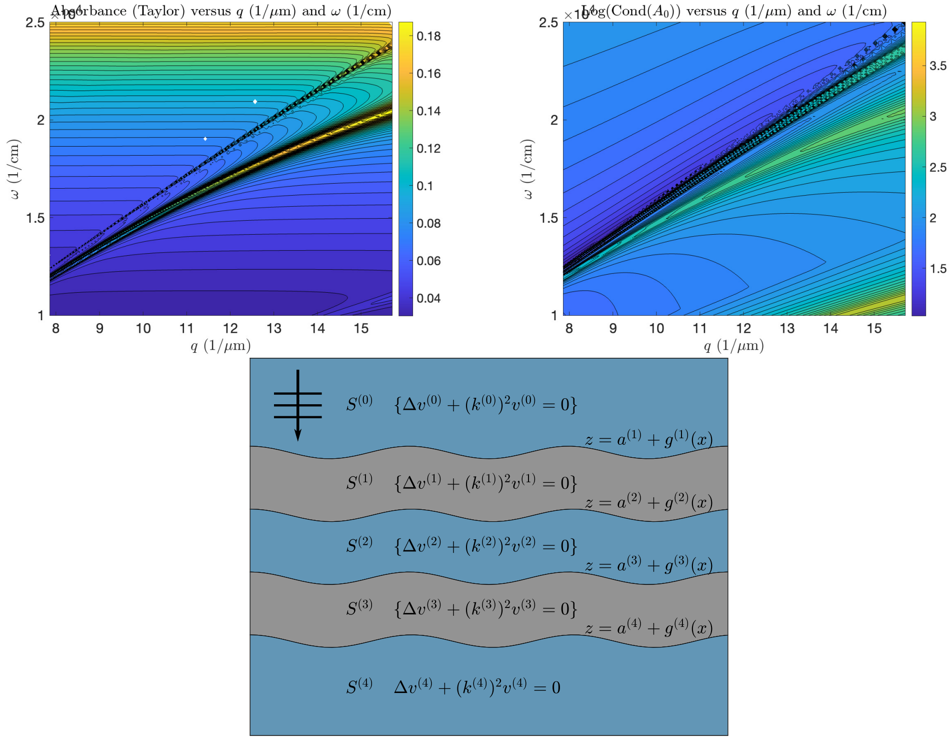

Fig. 17. (Above, left): Contour plot of absorbance as a function of wavenumber, q (inverse microns), and illumination frequency, ω (inverse centimeters), for a quintuply layered vacuum–silver structure with sinusoidal interfaces ($b_1 = b_3 = 1$, $b_2 = b_4 = 0$, $c_1 = c_3 = 0$, $c_2 = c_4 = 1$, $\kappa = 1 - 1/64$, $r = 64$), (18), of amplitude $\varepsilon = 0.002$ using Taylor summation. Physical parameters were (19) and numerical discretization was (20). (Above, right): Contour plot of the logarithm of the condition number of $\mathbf{A}_p$ which measures the singularity in $\mathbf{A}_p$ and the dispersion relation for this configuration. (Below): Plot of the grating structure.

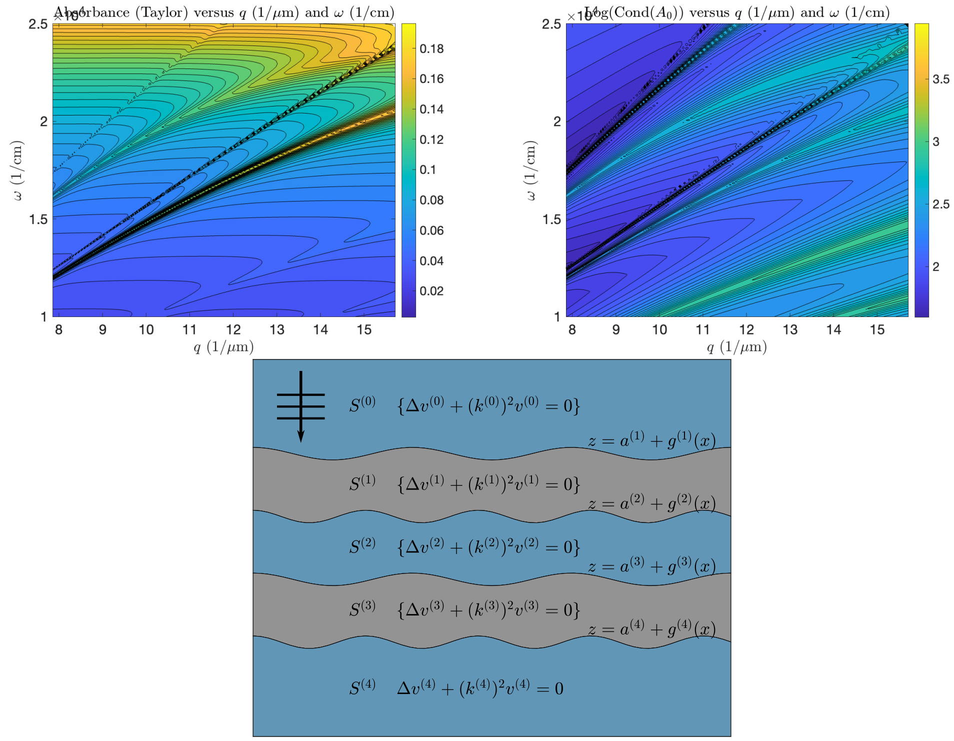

Fig. 18. (Above, left): Contour plot of absorbance as a function of wavenumber, q (inverse microns), and illumination frequency, ω (inverse centimeters), for a quintuply layered vacuum–silver structure with sinusoidal interfaces ($b_1 = b_3 = 1$, $b_2 = b_4 = 0$, $c_1 = c_3 = 0$, $c_2 = c_4 = 1$, $\kappa = 1 + \sqrt{2}$), (18), of amplitude $\varepsilon = 0.002$ using Taylor summation. Physical parameters were (19) and numerical discretization was (20). (Above, right): Contour plot of the logarithm of the condition number of $\mathbf{A}_p$ which measures the singularity in $\mathbf{A}_p$ and the dispersion relation for this configuration. (Below): Plot of the grating structure.

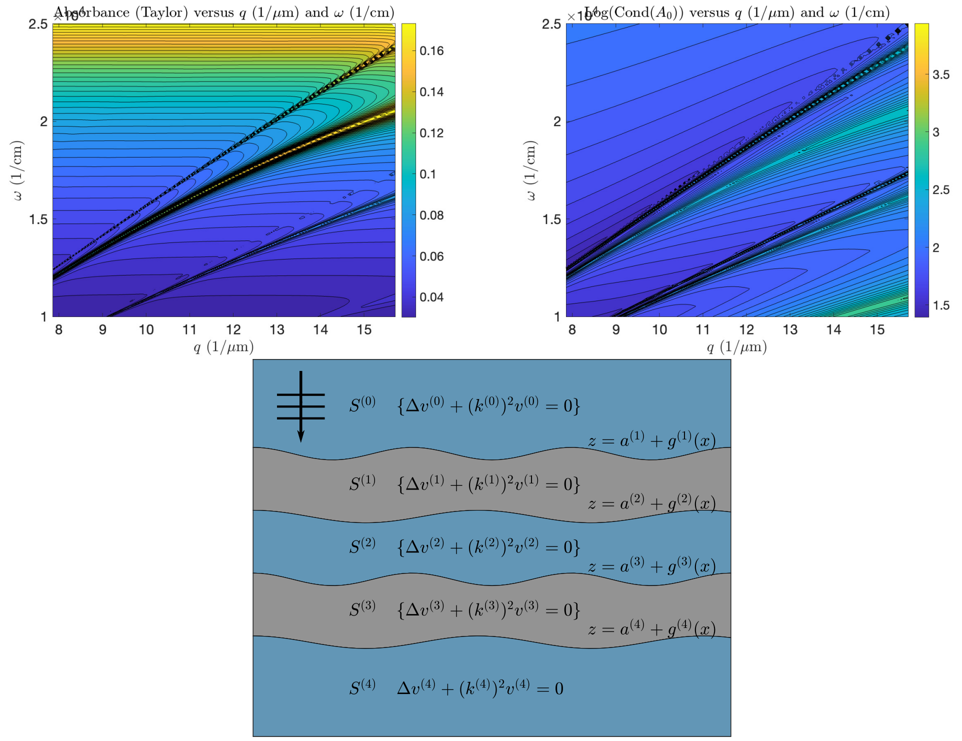

Fig. 19. (Above, left): Contour plot of absorbance as a function of wavenumber, q (inverse microns), and illumination frequency, ω (inverse centimeters), for a quintuply layered vacuum–silver structure with sinusoidal interfaces ($b_1 = b_3 = 1$, $b_2 = b_4 = 0$, $c_1 = c_3 = 0$, $c_2 = c_4 = 1$, $\kappa = 1 - \sqrt{2}$, (18), of amplitude $\varepsilon = 0.002$ using Taylor summation. Physical parameters were (19) and numerical discretization was (20). (Above, right): Contour plot of the logarithm of the condition number of $\mathbf{A}_p$ which measures the singularity in $\mathbf{A}_p$ and the dispersion relation for this configuration. (Below): Plot of the grating structure.

Acknowledgments

D.P.N. gratefully acknowledges support from the National Science Foundation through grant No. DMS–2111283.

Disclosures

The author declares no conflicts of interest.

Data Availability

Data underlying the results presented in this paper are not publicly available at this time but may be obtained from the author upon reasonable request.

References

1. J. D. Joannopoulos, P. R. Villeneuve, and S. Fan, "Photonic crystals: putting a new twist on light," Nature **386**, 143–149 (1997).
2. J. D. Joannopoulos, S. G. Johnson, J. N. Winn, and R. D. Meade, *Photonic Crystals: Molding the Flow of Light* (Princeton University Press, 2008), 2nd ed.
3. H. Raether, *Surface plasmons on smooth and rough surfaces and on gratings* (Springer, Berlin, 1988).
4. S. A. Maier, *Plasmonics: Fundamentals and Applications* (Springer, New York, 2007).
5. S. Enoch and N. Bonod, *Plasmonics: From Basics to Advanced Topics*, Springer Series in Optical Sciences (Springer, New York, 2012).
6. J. Homola, "Surface plasmon resonance sensors for detection of chemical and biological species," Chem. Rev. **108**, 462–493 (2008).
7. Y. Zhao, X. Hu, G. Chen, *et al.*, "Infrared biosensors based on graphene plasmonics: modeling," Phys. Chem. Chem. Phys. **15**, 17118 (2013).
8. J.-F. Masson, "Surface plasmon resonance clinical biosensors for medical diagnostics," ACS Sensors **2**, 16–30 (2017).
9. S.-H. Oh and H. Altug, "Performance metrics and enabling technologies for nanoplasmonic biosensors," Nat. Commun. **9**, 5263 (2018).
10. A. M. Shrivastav, U. Cvelbar, and I. Abdulhalim, "A comprehensive review on plasmonic-based biosensors used in viral diagnostics," Commun. Biol. **4**, 1–12 (2021).
11. J. Wekalao, M. S. Kumaresan, S. Mallan, *et al.*, "Metasurface based surface plasmon resonance (SPR) biosensor for cervical cancer detection with behaviour prediction using machine learning optimization based on support vector regression," Plasmonics (2024).
12. T. Springer, M. Bockova, J. Slaby, *et al.*, "Surface plasmon resonance biosensors and their medical applications," Biosens. Bioelectron. **278**, 117308 (2025).
13. G. Veronis and S. Fan, "Overview of simulation techniques for plasmonic devices," in *Surface Plasmon Nanophotonics,* vol. 131 of *Springer Series in Optical Sciences* (Springer, 2007), pp. 169–182.
14. B. Gallinet, J. Butet, and O. J. F. Martin, "Numerical methods for nanophotonics: Standard problems and future challenges," Laser Photonics Rev. **9**, 577–603 (2015).
15. A. Taflove and S. C. Hagness, *Computational electrodynamics: the finite-difference time-domain method* (Artech House, Inc., Boston, MA, 2000), 2nd ed.
16. R. Rumpf, *Electromagnetic and Photonic Simulation for the Beginner: Finite-Difference Frequency-Domain in MATLAB* (Artech House, Inc., Boston, MA, 2020).
17. J. Jin, *The finite element method in electromagnetics* (Wiley-Interscience [John Wiley & Sons], New York, 2002), 2nd ed.
18. K. Busch, M. König, and J. Niegemann, "Discontinuous Galerkin methods in nanophotonics," Laser & Photonics Rev. **5**, 773–809 (2011).
19. R. D. Meade, A. M. Rappe, K. D. Brommer, *et al.*, "Accurate theoretical analysis of photonic band-gap materials," Phys. Rev. B **48**, 8434–8437 (1993).
20. S. G. Johnson and J. D. Joannopoulos, "Block-iterative frequency-domain methods for Maxwell's equations in a planewave basis," Opt. Express **8**, 173–190 (2001).
21. M. G. Moharam and T. K. Gaylord, "Rigorous coupled-wave analysis of planar-grating diffraction," J. Opt. Soc. Am. **71**, 811–818 (1981).
22. P. Lalanne and G. M. Morris, "Highly improved convergence of the coupled-wave method for TM polarization," J. Opt. Soc. Am. A **13**, 779–784 (1996).
23. H. Kim, J. Park, and B. Lee, *Fourier modal method and its applications in computational nanophotonics* (CRC Press, Boca Raton, FL, 2012).
24. B. T. Draine and P. J. Flatau, "Discrete-dipole approximation for scattering calculations," J. Opt. Soc. Am. A **11**, 1491–1499 (1994).

25. D. Colton and R. Kress, *Inverse acoustic and electromagnetic scattering theory*, vol. 93 of *Applied Mathematical Sciences* (Springer, New York, 2013), 3rd ed.
26. W. Chew, J. Jin, E. Michielssen, and J. Song, *Fast and Efficient Algorithms in Computational Electromagnetics* (Artech House, 2001).
27. Y. Liu, *Fast Multipole Boundary Element Method: Theory and Applications in Engineering* (Cambridge University Press, 2009).
28. V. Rokhlin, "Rapid solution of integral equations of classical potential theory," J. Comput. Phys. **60**, 187–207 (1985).
29. L. Greengard and V. Rokhlin, "A fast algorithm for particle simulations," J. Comput. Phys. **73**, 325–348 (1987).
30. E. Darve and P. Havé, "A fast multipole method for Maxwell equations stable at all frequencies," Philos. Trans. R. Soc. Lond. Ser. A Math. Phys. Eng. Sci. **362**, 603–628 (2004).
31. A. M. Kern and O. J. F. Martin, "Surface integral formulation for 3d simulations of plasmonic and high permittivity nanostructures," J. Opt. Soc. Am. A **26**, 732–740 (2009).
32. D. M. Milder, "An improved formalism for rough-surface scattering of acoustic and electromagnetic waves," in *Proceedings of SPIE - The International Society for Optical Engineering (San Diego, 1991),* vol. 1558 (Int. Soc. for Optical Engineering, Bellingham, WA, 1991), pp. 213–221.
33. D. M. Milder, "An improved formalism for wave scattering from rough surfaces," J. Acoust. Soc. Am. **89**, 529–541 (1991).
34. D. M. Milder and H. T. Sharp, "Efficient computation of rough surface scattering," in *Mathematical and numerical aspects of wave propagation phenomena (Strasbourg, 1991),* (SIAM, Philadelphia, PA, 1991), pp. 314–322.
35. D. M. Milder and H. T. Sharp, "An improved formalism for rough surface scattering. ii: Numerical trials in three dimensions," J. Acoust. Soc. Am. **91**, 2620–2626 (1992).
36. D. M. Milder, "Role of the admittance operator in rough-surface scattering," J. Acoust. Soc. Am. **100**, 759–768 (1996).
37. D. M. Milder, "An improved formalism for electromagnetic scattering from a perfectly conducting rough surface," Rádió Sci. **31**, 1369–1376 (1996).
38. R. Coifman, M. Goldberg, T. Hrycak, *et al.*, "An improved operator expansion algorithm for direct and inverse scattering computations," Waves Random Media **9**, 441–457 (1999).
39. O. Bruno and F. Reitich, "Numerical solution of diffraction problems: A method of variation of boundaries," J. Opt. Soc. Am. A **10**, 1168–1175 (1993).
40. O. Bruno and F. Reitich, "Numerical solution of diffraction problems: A method of variation of boundaries. II. Finitely conducting gratings, Padé approximants, and singularities," J. Opt. Soc. Am. A **10**, 2307–2316 (1993).
41. O. Bruno and F. Reitich, "Numerical solution of diffraction problems: A method of variation of boundaries. III. Doubly periodic gratings," J. Opt. Soc. Am. A **10**, 2551–2562 (1993).
42. O. P. Bruno and F. Reitich, "Calculation of electromagnetic scattering via boundary variations and analytic continuation," Appl. Comput. Electromagn. Soc. J. **11**, 17–31 (1996).
43. O. P. Bruno and F. Reitich, "Boundary–variation solutions for bounded–obstacle scattering problems in three dimensions," J. Acoust. Soc. Am. **104**, 2579–2583 (1998).
44. O. P. Bruno and F. Reitich, "High-order boundary perturbation methods," in *Mathematical Modeling in Optical Science,* vol. 22 (SIAM, Philadelphia, PA, 2001), pp. 71–109. Frontiers in Applied Mathematics Series.
45. D. P. Nicholls and F. Reitich, "A new approach to analyticity of Dirichlet-Neumann operators," Proc. Roy. Soc. Edinb. Sect. A **131**, 1411–1433 (2001).
46. D. P. Nicholls and F. Reitich, "Stability of high-order perturbative methods for the computation of Dirichlet-Neumann operators," J. Comput. Phys. **170**, 276–298 (2001).
47. D. P. Nicholls and F. Reitich, "Analytic continuation of Dirichlet-Neumann operators," Numer. Math. **94**, 107–146 (2003).
48. D. P. Nicholls and F. Reitich, "Shape deformations in rough surface scattering: Cancellations, conditioning, and convergence," J. Opt. Soc. Am. A **21**, 590–605 (2004).
49. D. P. Nicholls and F. Reitich, "Shape deformations in rough surface scattering: Improved algorithms," J. Opt. Soc. Am. A **21**, 606–621 (2004).
50. D. P. Nicholls and F. Reitich, "Boundary perturbation methods for high–frequency acoustic scattering: Shallow periodic gratings," J. Acoust. Soc. Amer. **123**, 2531–2541 (2008).
51. D. P. Nicholls, "A method of field expansions for vector electromagnetic scattering by layered periodic crossed gratings," J. Opt. Soc. Am. A **32**, 701–709 (2015).
52. Y. He, D. P. Nicholls, and J. Shen, "An efficient and stable spectral method for electromagnetic scattering from a layered periodic structure," J. Comput. Phys. **231**, 3007–3022 (2012).
53. Y. He, M. Min, and D. P. Nicholls, "A spectral element method with transparent boundary condition for periodic layered media scattering," J. Sci. Comput. **68**, 772–802 (2016).
54. Y. Hong and D. P. Nicholls, "A stable high-order perturbation of surfaces method for numerical simulation of diffraction problems in triply layered media," J. Comput. Phys. **330**, 1043–1068 (2017).
55. Y. Hong and D. P. Nicholls, "A high–order perturbation of surfaces method for scattering of linear waves by periodic multiply layered gratings in two and three dimensions," J. Comput. Phys. **345**, 162–188 (2017).
56. Y. Hong and D. P. Nicholls, "A high–order perturbation of surfaces method for vector electromagnetic scattering by doubly layered periodic crossed gratings," J. Comput. Phys. **372**, 748–772 (2018).

57. D. P. Nicholls and J. Shen, "A rigorous numerical analysis of the transformed field expansion method," SIAM J. on Numer. Anal. **47**, 2708–2734 (2009).
58. Y. Hong and D. P. Nicholls, "A rigorous numerical analysis of the transformed field expansion method for diffraction by periodic, layered structures," SIAM J. on Numer. Anal. **59**, 456–476 (2021).
59. G. A. Baker, Jr. and P. Graves-Morris, *Padé approximants* (Cambridge University Press, Cambridge, 1996), 2nd ed.
60. P. Chengfeng, Z. Shutao, M. Farsari, *et al.*, "Nanofabrication: the unsung hero in enabling advances in nanophotonics," Nanophotonics **12**, 1359–1361 (2023).
61. R. Bistritzer and A. H. MacDonald, "Moiré bands in twisted double-layer graphene," Proc. National Acad. Sci. **108**, 12233–12237 (2011).
62. D. Wong, K. P. Nuckolls, M. Oh, *et al.*, "Cascade of electronic transitions in magic-angle twisted bilayer graphene," Nature **582**, 198–202 (2020).
63. E. Andrei, D. Efetov, P. Jarillo-Herrero, *et al.*, "The marvels of Moiré materials," Nat. Rev. Mater. **6**, 201–206 (2021).
64. A. Uri, S. C. de la Barrera, M. T. Randeria, *et al.*, "Superconductivity and strong interactions in a tunable Moiré quasicrystal," Nature **620**, 762–767 (2023).
65. X. Lai, G. Li, A. M. Coe, *et al.*, "Moiré periodic and quasiperiodic crystals in heterostructures of twisted bilayer graphene on hexagonal boron nitride," Nat. Mater. (2025).
66. B. Lou and S. Fan, "RCWA4D: Electromagnetic solver for layered structures with incommensurate periodicities," Comput. Phys. Commun. **306**, 109356 (2025).
67. J. Moser, "On the theory of quasiperiodic motions," SIAM Rev. **8**, 145–172 (1966).
68. J. Wilkening and X. Zhao, "Quasi-periodic travelling gravity–capillary waves," J. Fluid Mech. **915**, Paper No. A7, 35 (2021).
69. J. Wilkening and X. Zhao, "Spatially quasi-periodic water waves of infinite depth," J. Nonlinear Sci. **31**, Paper No. 52, 43 (2021).
70. J. Wilkening and X. Zhao, "Spatially quasi-periodic bifurcations from periodic traveling water waves and a method for detecting bifurcations using signed singular values," J. Comput. Phys. **478**, Paper No. 111954, 34 (2023).
71. J. Wilkening and X. Zhao, "Spatially quasi-periodic water waves of finite depth," Proc. A. **479**, Paper No. 20230019, 28 (2023).
72. D. P. Nicholls, J. Wilkening, and X. Zhao, "Analyticity and stable computation of Dirichlet–Neumann operators for Laplace's equation under quasiperiodic boundary conditions in two and three dimensions," Stud. Appl. Math. (to appear) (2025).
73. D. P. Nicholls, "A method of field expansions for doubly layered media with a quasiperiodic interface," J. Opt. Soc. Am. A (submitted) (2025).
74. D. P. Nicholls, S.-H. Oh, T. W. Johnson, and F. Reitich, "Launching surface plasmon waves via vanishingly small periodic gratings," J. Opt. Soc. Am. A **33**, 276–285 (2016).
75. N. Lassaline, R. Brechbühler, S. Vonk, *et al.*, "Optical Fourier surfaces," Nature **582**, 506–510 (2020).
76. P. Yeh, *Optical waves in layered media*, vol. 61 (Wiley-Interscience, 2005).
77. G. Bao and P. Li, *Maxwell's equations in periodic structures*, vol. 208 of *Applied Mathematical Sciences* (Springer, Singapore; Science Press Beijing, Beijing, [2022] ©2022).
78. D. Gottlieb and S. A. Orszag, *Numerical analysis of spectral methods: theory and applications* (Society for Industrial and Applied Mathematics, Philadelphia, Pa., 1977). CBMS-NSF Regional Conference Series in Applied Mathematics, No. 26.
79. C. Canuto, M. Y. Hussaini, A. Quarteroni, and T. A. Zang, *Spectral methods in fluid dynamics* (Springer-Verlag, New York, 1988).
80. J. P. Boyd, *Chebyshev and Fourier spectral methods* (Dover Publications Inc., Mineola, NY, 2001), 2nd ed.
81. J. Shen, T. Tang, and L.-L. Wang, *Spectral methods*, vol. 41 of *Springer Series in Computational Mathematics* (Springer, Heidelberg, 2011). Algorithms, analysis and applications.
82. D. P. Nicholls, "A high–order spectral algorithm for the numerical simulation of layered media with uniaxial hyperbolic materials," J. Comput. Phys. **453**, 110961 (2022).
83. C. M. Bender and S. A. Orszag, *Advanced mathematical methods for scientists and engineers* (McGraw-Hill Book Co., New York, 1978). International Series in Pure and Applied Mathematics.
84. O. R. Burggraf, "Analytical and numerical studies of the structure of steady separated flows," J. Fluid Mech. **24**, 113–151 (1966).
85. P. J. Roache, "Code verification by the method of manufactured solutions," J. Fluids Eng. **124**, 4–10 (2002).
86. C. J. Roy, "Review of code and solution verification procedures for computational simulation," J. Comp. Phys. **205**, 131–156 (2005).
87. J. D. Jackson, *Classical electrodynamics* (John Wiley & Sons Inc., New York, 1975), 2nd ed.
88. R. J. LeVeque, *Finite difference methods for ordinary and partial differential equations* (Society for Industrial and Applied Mathematics (SIAM), Philadelphia, PA, 2007). Steady-state and time-dependent problems.
89. M. S. Gockenbach, *Understanding and implementing the finite element method* (Society for Industrial and Applied Mathematics (SIAM), Philadelphia, PA, 2006).